Geoderma 446 (2024) 116904

Contents lists available at ScienceDirect

Geoderma

journal homepage: www.elsevier.com/locate/geoderma

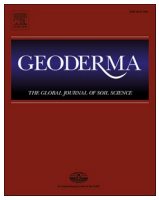

Contrasting stocks and origins of particulate and mineral-associated soil organic carbon in a mangrove-salt marsh ecotone

Prakhin Assavapanuvat [a,*], Joshua L. Breithaupt [b], Kevin M. Engelbert [b], Christian Schröder [c], Joseph M. Smoak [d], Thomas S. Bianchi [a]

[a] Department of Geological Sciences, University of Florida, Gainesville, FL, USA
[b] Coastal and Marine Laboratory, Florida State University, St. Teresa, FL, USA
[c] Biological and Environmental Sciences, University of Stirling, Stirling, Scotland, UK
[d] School of Geosciences, University of South Florida, St. Petersburg, FL, USA

ARTICLE INFO

Handling Editor: C. Rumpel

Keywords:
Mineral-associated organic carbon
Iron-bound organic carbon
Reactive iron
Mangrove
Salt marsh
Soil organic carbon fraction

ABSTRACT

The global warming-driven poleward expansion of mangrove habitats (e.g., *Avicennia germinans* and *Rhizophora mangle*) into temperate salt marshes (e.g., *Spartina alterniflora* and *Juncus roemerianus*) has been shown to alter coastal soil organic carbon (SOC) storage. However, the taxa-specific consequences of this vegetation shift on the origin and size of SOC sub-fractions (particulate OC (POC); mineral-associated OC (MAOC); and reactive iron-associated OC (FeR-MAOC)) remain largely unexplored. In this study, we used a particle size-based SOC fractionation method to compare quantity and $\delta^{13}C$ composition of bulk and each SOC sub-fractions in soil cores collected from Apalachicola Bay barrier islands in Florida, USA, the highest latitude where monospecific communities of all four aforementioned plants co-occur. Depth-dependent variation of bulk soil $\delta^{13}C$ clearly showed the global warming-driven replacement of *S. alterniflora* by mangroves, as well as reciprocal substitutions of *S. alterniflora* and *J. roemerianus*, probably driven by changes in wetland elevation. Higher OC burial rates in mangrove habitats suggested that mangrove soils were principally developed by particle deposition. In contrast, comparatively lower OC burial rates but higher OC stocks in salt marsh habitats illustrated subsurface OC input from salt marsh roots. POC was primarily derived from contemporary plant detritus; its concentration was higher in salt marsh habitats (58.8 ± 9.0 % of SOC) relative to mangroves (38.4 ± 6.0 % of SOC). In contrast, MAOC content did not vary across plant habitats (53.5 ± 10.9 % of SOC), and principally originated from microbially-transformed OC and pre-existing plants. FeR-MAOC was essentially absent in *R. mangle* soils (2.9 ± 3.6 % of SOC) while representing a minor fraction of MAOC in three other plant habitats (7.8 ± 7.0 % of SOC). The $\delta^{13}C$ of FeR-MAOC was more like the present-day surface plants, highlighting the in situ FeR-MAOC formation in their active oxidizing rhizospheres.

1. Introduction

Coastal intertidal vegetated habitats, which include salt marshes, mangroves, and coastal seagrasses, are considered to be important sites of CO_2 sequestration and organic carbon (OC) storage (i.e., blue carbon) (e.g., Macreadie et al., 2021 and references therein). In salt marsh and mangrove habitats, approximately 95 and 71 % of the total OC stock is stored in soils (Alongi, 2020), accounting for 0.4 to 6.5 and 9.4 to 10.4 Pg of the global soil organic carbon (SOC) stock, respectively (Duarte et al., 2013). Nevertheless, there remains some uncertainties on the stability of SOC in coastal wetlands, as these systems may also be sources of greenhouse gases in certain regions, due to SOC decomposition (Rosentreter et al., 2023). Consequently, there is need for a better understanding on how key environmental drivers (e.g., relative sea-level rise, plant-species effects) impact SOC formation and preservation across latitudinal gradients (Breithaupt and Steinmuller, 2022; Lovelock and Reef, 2020; Spivak et al., 2019).

Due to climate warming, some low-latitude coastal vegetation communities are expanding their habitats poleward. The replacement of temperate salt marshes by mangroves is occurring worldwide (e.g., Osland et al., 2017b; Quisthoudt et al., 2012), including the USA (Osland et al., 2021), Australia (Kelleway et al., 2016), and South Africa

* Corresponding author at: Department of Geological Sciences, University of Florida, 241 Williamson Hall, PO Box 112120, Gainesville, Florida 32611-2120, USA.
E-mail address: assavapanuvat.p@ufl.edu (P. Assavapanuvat).

https://doi.org/10.1016/j.geoderma.2024.116904
Received 7 December 2023; Received in revised form 30 April 2024; Accepted 2 May 2024

(Geldenhuys et al., 2016). In North America, mangrove-salt marsh replacements on the western seaboard have been regulated by rainfall and temperature regimes, while those on the Atlantic coast and the northern-to-eastern Gulf of Mexico have been primarily controlled by the frequency of extreme freezing events (e.g., Bardou et al., 2021; Cavanaugh et al., 2014; McKee and Rooth, 2008; Osland et al., 2020, 2019, 2017a, 2017b). Coastal vegetation shifts are expected to change coastal OC dynamics via alterations in OC composition, sedimentation rates, soil hydrology, soil redox state, and plant-microbial interactions (Spivak et al., 2019). These combined effects can lead to a multitude of responses in SOC stocks and/or burial rates such as, increases (e.g.., Bianchi et al., 2013; Breithaupt et al., 2020; Mcleod et al., 2011; Radabaugh et al., 2023, 2018; Vaughn et al., 2020), no change (e.g., Dontis et al., 2020; Doughty et al., 2016; Duarte et al., 2005; Simpson et al., 2021; Steinmuller et al., 2022b), and even decreases (e.g., Steinmuller et al., 2020), all depending on site-specific conditions. This highlights the need for more studies on plant-specific effects on SOC stabilization in transitional zones, to better predict changes in coastal wetland SOC stocks under a warming climate.

Organo-mineral associations have long been thought to be an important mechanism for the stabilization and preservation of OC in soils and sediments (e.g., Kleber et al., 2021; Ransom et al., 1998). This has led to the development of soil organic matter fractionation schemes to separate particulate organic matter (POM) and mineral-associated organic matter (MAOM) (e.g., Cambardella and Elliott, 1992; Lavallee et al., 2020; Poeplau et al., 2018). Large and low-density unprotected organic detritus is operationally defined as POM, while small and heavy organic matter associated with reactive mineral surfaces is defined as MAOM (see list of all abbreviations in Table 1). Much of the particulate organic carbon (POC) in soil is plant-derived and largely comprised of recalcitrant complex organic molecules (e.g., lignocellulose) (Angst et al., 2021; Lavallee et al., 2020, 2018). In contrast, mineral-associated organic carbon (MAOC) is believed to originate from microbial-derived OC (a.k.a. in vivo pathway) and/or plant-derived labile OC, such as rhizodeposits, (a.k.a. ex vivo pathway) (Angst et al., 2021; Cotrufo et al., 2015; Lavallee et al., 2020; Sokol et al., 2019; Villarino et al., 2021). One of the most important groups of soil minerals that can stabilize OC is reactive iron (FeR). FeR has been operationally defined as sodium dithionite-reducible iron (oxy)hydroxides (Lalonde et al., 2012), which is different from the classical definition of reactive iron in marine sediments as a fraction of iron readily reacts with sulfide to form various iron sulfide minerals (Canfield, 1989). The formation of reactive iron-associated OC (FeR-MAOC) is an important OC stabilization mechanism in terrestrial, coastal, and marine settings (e.g., Chen et al., 2024; Lalonde et al., 2012; Li et al., 2023; Shields et al., 2016; Ye et al., 2022; Zhao et al., 2016).

Due to differences in their origins and composition, the stability of POC is dependent on its intrinsic chemical recalcitrance and the potential for the inhibition of microbial enzymes under oxygen-depleted redox conditions (Lavallee et al., 2020), while the persistence of MAOC is regulated by the chemical stabilization of soil minerals (Lavallee et al., 2020; Sokol et al., 2022). For instance, FeR-MAOC is generally stabilized under oxic conditions, but destabilized under anoxic conditions, due to different solubility properties of reduced and oxidized iron (e.g., Chen et al., 2020; Dong et al., 2023; Kida and Fujitake, 2020). In coastal wetland soils, previous studies have estimated a broad range of POC, MAOC, and FeR-MAOC fractions (Table 2 and 3). This large variation may depend on different extraction methods (e.g., particle size versus density), different plant productivity across latitudinal gradients (e.g., Fu et al., 2024), site-specific hydrodynamic factors, and species-specific influences of plants. The latter is not only regulated by broad plant groups (e.g., mangrove versus salt marsh), but also taxon-specific effects (e.g., *A. germinans* mangrove versus *R. mangle* mangrove). For example, the enrichment of recalcitrant organic compounds (e.g., lignin and tannins) in *R. mangle* mangrove detritus (Friesen et al., 2018; Saraswati et al., 2016) may promote the accumulation of POC. In contrast, increasing soil redox potential (Eh) due to oxygen release from *A. germinans* mangrove rhizosphere (Comeaux et al., 2012; Friesen et al., 2018; Krauss et al., 2006; Perry and Mendelssohn, 2009; Thibodeau and Nickerson, 1986) may facilitate FeR-MAOC formation. Since the direct influence of plants can often be overshadowed by environmental factors from larger regional gradients (Breithaupt and Steinmuller, 2022; Steinmuller et al., 2022b), our study aims to investigate the effects of plant species on the formation of SOC sub-fractions in a small system (~500 × 300 m^2) where regional variabilities are minimized.

Here, we hypothesize that mangrove-salt marsh transition will impact the quantity and composition of bulk SOC and its respective sub-fractions (POC, MAOC, FeR-MAOC). To test this hypothesis, our

Table 1
Summary of terminologies, abbreviations, and operational definitions of soil OC sub-fractions.

Terminology	Abbreviation	Definition	References
Bulk soil total organic carbon	OC_{Bulk}	Total amount of organic carbon measured in bulk soil samples (% of dry soil weight)	Harris et al. (2001)
Particulate organic carbon (i.e., shredded plant detritus)	POC	Soil organic carbon with particle size larger than 53 μm and lower density than 1.85 g cm^{-3}	Cambardella and Elliott (1992) Cotrufo et al. (2019)
	POC content	Weight of POC (g) stored in 100 g of dry soil	
	f_{POC}	Fraction of OC_{Bulk} classified as POC (% of OC_{Bulk})	
Mineral-associated organic carbon	MAOC	Soil organic carbon with particle size smaller than 53 μm and higher density than 1.85 g cm^{-3}	Cambardella and Elliott (1992) Cotrufo et al. (2019)
	MAOC content	Weight of MAOC (g) stored in 100 g of dry soil	
	f_{MAOC}	Fraction of OC_{Bulk} classified MAOC (% of OC_{Bulk})	
Post-control extracted OC	$OC_{Control}$	OC that remained in residual solid after bulk soil was treated with 1.6 M sodium chloride + 0.11 M sodium bicarbonate solution	Lalonde et al. (2012)
Citrate Bicarbonate Dithionite extracted organic carbon	OC_{CBD}	OC that remained in residual solid after $OC_{Control}$ was treated with 0.27 M trisodium citrate + 0.11 M sodium bicarbonate solution	Lalonde et al. (2012)
Reactive iron mineral-associated organic carbon	FeR-MAOC	Difference between $OC_{Control}$ and OC_{CBD}	Lalonde et al. (2012)
	FeR-MAOC content	Weight of FeR-MAOC (g) stored in 100 g of dry soil	
	$f_{FeR\text{-}MAOC}$	Fraction of OC_{Bulk} classified as FeR-MAOC (% of OC_{Bulk})	
Non-reactive iron mineral-associated organic carbon	nonFeR-MAOC	Difference between MAOC and FeR-MAOC	Lalonde et al. (2012)
	nonFeR-MAOC content	Weight of nonFeR-MAOC (g) stored in 100 g of dry soil	
	$f_{nonFeR\text{-}MAOC}$	Fraction of OC_{Bulk} classified as nonFeR-MAOC (% of OC_{Bulk})	

Table 2
Summary of previous studies on the fractionation of coastal wetland SOC into size and/or density fractions (a.k.a. MAOC and POC separation). Unless specified, the number in POC columns represents the particle size fraction > 53 μm and/or density < 1.85 g cm^{-3}. The number in MAOC columns represents the particle size fraction < 53 μm and/or density > 1.85 g cm^{-3}. While %OC of each SOC fraction in most studies were measured by Elemental Analyzers, the asterisk in the method column marks specific studies that used dichromate oxidation method for %OC measurement. The order of studies is ranked from highest to lowest latitudes.

Study	Method	Location	Plant habitats	Fraction (% of SOC)		Content (gC per Kg soil, or specified)	
				POC	MAOC	POC	MAOC
Fu et al. (2024)	Only size	Across Chinese eastern coastline	Mangroves	**0–20 cm:** 49.4 ± 24.9 **0–100 cm:** 36.5 ± 21.1	**0–20 cm:** 51.6 ± 24.9 **0–100 cm:** 63.5 ± 21.1	**0–100 cm:** 8.8 ± 7.2	**0–100 cm:** 10.5 ± 7.1
			Salt marshes	**0–20 cm:** 21.1 ± 19.0 **0–100 cm:** 13.6 ± 7.8	**0–20 cm:** 78.9 ± 19.0 **0–100 cm:** 86.4 ± 7.8	**0–100 cm:** 1.5 ± 2.0	**0–100 cm:** 6.6 ± 4.1
Komada et al. (2022)	Only density **Free low density:** < 1.6 g cm^{-3} without sonication **Occluded low density:** < 1.6 g cm^{-3} with sonication **Meso-density:** 1.6–2.5 g cm^{-3} **High density:** > 2.5 g cm^{-3}	San Francisco Bay, California, USA (0–50 cm depth)	*Spartina* spp.	**Free low density:** 4–20 **Occluded low density:** 2–25	**Meso-density:** 26–73 **High-density:** 1–6	**Free low density:** 30–430 **Occluded low density:** 30–260	**Meso-density:** 5–27 **High-density:** ≤ 2
Sun et al. (2023)	Only size	Yellow River Estuary, Shandong, China	Salt marshes (Mixed species without *S. alterniflora*)	–	–	**0–10 cm:** 1.4–3.2 **20–40 cm:** 0.2–0.3	**0–10 cm:** 1.7–3.4 **20–40 cm:** 0.6–0.7
Ma et al. (2024)	*Only size, no aggregate destruction	Dongying, Shandong, China	*S. salsa* (natural)	–	–	–	**0–10 cm:** 3.18 ± 0.84 **40–60 cm:** 2.53 ± 0.29
			S. salsa (regenerated)	–	–	–	**0–10 cm:** 3.00 ± 0.36 **40–60 cm:** 2.45 ± 0.52
Yang et al. (2016)	Size & density **Ligh fraction:** < 1.7 g cm^{-3} **Intra-aggregate:** > 53 μm, > 1.7 g cm^{-3} **Heavy fraction:** < 53 μm, > 1.7 g cm^{-3}	Yancheng, Jiangsu, China (30 cm depth)	Mud flat	**Light fraction:** 6 **Intra-aggregate:** 39	**Heavy fraction:** 53	**Light fraction:** 28 ± 7 gC m^{-2} **Intra-aggregate:** 177 ± 6 gC m^{-2}	**Heavy fraction:** 236 ± 9 gC m^{-2}
			S. alterniflora (10-year-old)	**Light fraction:** 2 **Intra-aggregate:** 41	**Heavy fraction:** 57	**Light fraction:** 71 ± 5 gC m^{-2} **Intra-aggregate:** 1547 ± 90 gC m^{-2}	**Heavy fraction:** 2153 ± 157 gC m^{-2}
			S. salsa	**Light fraction:** 4 **Intra-aggregate:** 25	**Heavy fraction:** 71	**Light fraction:** 83 ± 16 gC m^{-2} **Intra-aggregate:** 503 ± 59 gC m^{-2}	**Heavy fraction:** 1450 ± 122 gC m^{-2}
			P. australis	**Light fraction:** 4 **Intra-aggregate:** 26	**Heavy fraction:** 53	**Light fraction:** 74 ± 15 gC m^{-2} **Intra-aggregate:** 441 ± 61 gC m^{-2}	**Heavy fraction:** 1158 ± 62 gC m^{-2}
Yang et al. (2017)	Size & density **Light fraction:** < 1.7 g cm^{-3} **Intra-aggregate:** > 53 μm, > 1.7 g cm^{-3} **Heavy fraction:** < 53 μm, > 1.7 g cm^{-3}	Yancheng, Jiangsu, China (0–30 cm depth)	*S. alterniflora* (6-year-old)	**Light fraction:** 4 **Intra-aggregate:** 38	**Heavy fraction:** 59	**Light fraction:** 115 ± 16 gC m^{-2} **Intra-aggregate:** 1234 ± 303 gC m^{-2}	**Heavy fraction:** 1923 ± 399 gC m^{-2}
			S. alterniflora (17-year-old)	**Light fraction:** 3 **Intra-aggregate:** 50	**Heavy fraction:** 47	**Light fraction:** 153 ± 11 gC m^{-2} **Intra-aggregate:** 2531 ± 64 gC m^{-2}	**Heavy fraction:** 2384 ± 33 gC m^{-2}
			S. alternniflora (20-year-old)	**Light fraction:**4 **Intra-aggregate:** 44	**Heavy fraction:** 52	**Light fraction:** 154 ± 11 gC m^{-2} **Intra-aggregate:** 1897 ± 177 gC m^{-2}	**Heavy fraction:** 2224 ± 158 gC m^{-2}
Zhang et al. (2024)	Only size	Xiaoyangkou estuary, Jiangsu, China	Mud flat	**0–20 cm:** 6.79–26.11 **80–100 cm:** 7.13–28.48	**0–20 cm:** 73.89–93.21 **80–100 cm:** 71.52–92.87	**0–20 cm:** 1.89–3.57 **80–100 cm:** 1.55–3.60	**0–20 cm:** 10.48–13.31 **80–100 cm:** 10.30–11.18
			S. alterniflora	**0–20 cm:** 14.29–29.23 **80–100 cm:** 15.43–38.02	**0–20 cm:** 70.77–85.71 **80–100 cm:** 61.98–84.54	**0–20 cm:** 1.05–2.63 **80–100 cm:** 1.69–3.60	**0–20 cm:** 10.15–10.70 **80–100 cm:** 9.55–10.52

(*continued on next page*)

Table 2 (*continued*)

Study	Method	Location	Plant habitats	Fraction (% of SOC)		Content (gC per Kg soil, or specified)	
				POC	MAOC	POC	MAOC
This study	Only size	Apalachicola river barrier island	*A. germinans*	**0–45 cm:** 39.63 ± 10.33	**0–45 cm:** 60.37 ± 10.33	**0–45 cm:** 30.3 ± 17.5	**0–45 cm:** 41.9 ± 9.9
			R. mangle	**0–45 cm:** 35.53 ± 11.18	**0–45 cm:** 64.47 ± 11.18	**0–45 cm:** 19.8 ± 9.1	**0–45 cm:** 37.0 ± 13.9
			S. alterniflora	**0–45 cm:** 57.85 ± 15.62	**0–45 cm:** 42.15 ± 15.62	**0–45 cm:** 43.4 ± 27.7	**0–45 cm:** 32.6 ± 19.3
			J. roemerianus	**0–45 cm:** 59.07 ± 9.53	**0–45 cm:** 40.93 ± 9.53	**0–45 cm:** 43.3 ± 21.1	**0–45 cm:** 32.4 ± 20.2
Mirabito and Chambers (2023)	Size & Density **Light fraction:** < 1.85 g cm^{-3} **Heavy fraction:** > 1.85 g cm^{-3}	Louisiana, USA (0–50 cm depth)	*S. alterniflora*	**Light (>2 mm):** 36.42 **Light (2 mm-25 μm):** 15.13 **Light (25–53 μm):** 13.63 **Light (<53 μm):** 6.07	**Heavy (>2mm):** 2.04 **Heavy (2 mm-25 μm):** 1.07 **Heavy (25–53 μm):** 1.04 **Heavy (<53 μm):** 24.60	**Light (>2 mm):** 39.40 ± 3.08 **Light (2 mm-25 μm):** 16.36 ± 2.11 **Light (25–53 μm):** 14.74 ± 3.01 **Light (<53 μm):** 6.56 ± 1.74	**Heavy (>53 μm):** NA **Heavy (<53 μm):** 26.60 ± 1.07
Feng et al. (2019)	*Only size, no aggregate destruction	Qi'ao island, Guangdong, China	*K. obovata* (native)	**0–20 cm:** ~70 **20–50 cm:** ~75	–	**0–20 cm:** 45 **20–50 cm:** 15	–
			S. alterniflora (encroached) & *S. apetala* (replanted)	**0–50 cm:** 75	–	**0–50 cm:** 15	–
Chen et al. (2023)	Only density	Qi'ao island, Guangdong, China	Afforested mangroves	**0–100 cm:** 7.0–15.1	**0–100 cm:** 84.9–93.0	**0–100 cm:** 24.2–35.8	**0–100 cm:** 11.9–16.5
Zhang et al. (2021)	*Only size	Zhangjiang, Guangxi, China	Mud flat	**0–60 cm:** 15.87	–	–	–
			Mangroves	**0–60 cm:** 25.8–41.4, up to 65.11 seaward	–	–	–
Jimenez et al. (2021)	Soil demineralization method (HF)	Cocó river estuary, Brazil	Living-dead mangroves	–	**0–40 cm:** 30–60	–	–

objectives were as follows: 1) determine the bulk SOC stock and burial rate in recently established mangroves (*A. germinans* and *R. mangle*) and native salt marshes (*S. alterniflora* and *J. roemerianus*) habitats; 2) compare relative abundance of POC, MAOC, and FeR-MAOC; and 3) identify down-core shifts in OC sources in bulk and sub-fractions of SOC, using bulk carbon stable isotopic ratios ($\delta^{13}C$).

2. Materials and methods

2.1. Study site

Sampling was conducted within the Pilot's Cove area on Little St. George Island in the Apalachicola Bay region in northwestern Florida, USA (Fig. 1). This region is the highest latitude in the Gulf of Mexico where both *Avicennia germinans* (black mangrove) and *Rhizophora mangle* (red mangrove) maintain monospecific communities and encroach into the monospecific communities of *Spartina alterniflora* and *Juncus roemerianus* salt marshes (Bardou et al., 2021; Snyder et al., 2021). Based on historical records, the first occurrence of *A. germinans* in this region was recorded in 1941 on Dog Island, approximately 50 km northeast of our study site, while *R. mangle* was firstly recorded on St. George Island in 2003. The first record of *A. germinans* and *R. mangle* on Little St. George Island, our study site, was documented in 1986 and 2008, respectively (Snyder et al., 2021). Soils in Pilot's Cove were classified as Terric Sulfisaprists (Dirego series) and Cumulic Endoaquolls (Bayvi series) (United States Department of Agriculture, 2023). Apalachicola Estuary barrier islands are experiencing a relative sea-level rise of 2.93 ± 0.58 mm yr^{-1} from 1967 to 2022 (NOAA, Tides and Currents Station 8728690). This region has also experienced multiple hurricane events. For example, Hurricane Dennis (2005) partially destroyed coastal plant communities (Edmiston et al., 2008), while Hurricane Michael (2018) triggered substantial soil surface elevation loss at Pilot's Cove (Steinmuller et al., 2022a).

2.2. Sample collection

Twelve soil cores (3 cores from each of the four plant habitats) were collected from Pilot's Cove on March 13th (cores mAG1 and mRM1) and August 27th, 2021 (the remaining cores; Fig. 1). A polyvinylchloride corer, with 10.16-cm interior diameter, was hammered into the soil down to maximum depth of 45 cm, unless a sand layer impeded further penetration. *A. germinans* soil cores were collected within 1-m radius of an *A. germinans* main trunk, while *R. mangle* soil cores were sampled as close to the main trunk as possible, within the constraints imposed by mangrove prop roots. *J. roemerianus* and *S. alterniflora* soil cores were collected from monospecific regions of each salt marsh taxon. Three replicate soil cores of each plant type were retrieved from different plant colonies (>50 m distance) to reduce the risk of spatial autocorrelation. Two soil cores, from each of the four plant habitats, were sub-sectioned in 1-cm intervals, and used for bulk analyses, MAOC-POC separation, and FeR-MAOC extraction. Another soil core from each plant habitat (mAG2, mRM2, sSA1, and sJR1) was divided into 5-cm intervals, their bulk soil $\delta^{13}C$ was firstly reported by Steinmuller et al., (2022b). All soil samples were freeze-dried prior to all chemical analyses. Shells, gravel, and plant detritus larger than 2 mm were removed prior to homogenization by mortar and pestle.

2.3. Bulk elemental and stable isotope analyses

Bulk elemental (C and N) and associated stable isotopic measurements were performed on homogenized soil samples from 3 soil cores of each plant habitat (total n = 286), using Carlo Erba 1500 CN elemental

Table 3
Summary of $f_{FeR\text{-}MAOC}$ in coastal wetland soils reported in previous studies. The order of studies are ranked from highest to lowest latitudes. For the additional references of $f_{FeR\text{-}MAOC}$ in terrestrial and marine environments, please see the reviews in Li et al. (2023) and Chen et al. (2024).

Study	Location	Depth	Plant habitats	$f_{FeR\text{-}MAOC}$ (% of SOC)
Duan et al. (2020)	Honghe national nature reserve, Heilongjiang, China (Freshwater wetland)	0–20 cm	*C. augustifolia* & *C. lasiocarpa* Rhizospheric soil	13–23
			Soils outside rhizosphere	1–11
Chen et al. (2024)	Yancheng, Jiangsu, China	0–50 cm	Mud flat	8.0–9.7
			S. alterniflora (since 1989)	13.9–15.8
			S. alterniflora (since 2003)	16.3–18.8
			S. salsa	7.0–8.7
			P. australis	5.9–15.1
Lin et al. (2023)	Chongming island, Hengsha island, and Minjiang river estuary, China	0–10 cm	*S. alterniflora*	2–13
			P. australis	7–10
This study	Apalachicola river barrier island	0–45 cm	*A. germinans*	8.33 ± 6.28
			R. mangle	2.92 ± 3.60
			S. alterniflora	7.86 ± 8.06
			J. roemerianus	7.36 ± 6.85
Shields et al. (2016)	Wax Lake Delta, Louisiana, USA	0–50 cm	*C. esculenta* & *S. nigra* (subaerial for13 years)	8.1 ± 3.2
			C. esculenta & *S. nigra* (subaerial for 26 years)	20.2 ± 3.8
			C. esculenta & *S. nigra* (subaerial for 38 years)	15.0 ± 4.3
Bai et al. (2021)	Tajiaozhou wetland, Fujian, China	0–10 cm	*C. malaccensis* (low salinity site)	18–20
	Bianfuzhou wetland, Fujian, China		*C. malaccensis* (medium salinity)	16–34
	Shanyutan wetland, Fujian, China		*C. malaccensis* (high salinity)	26–32
Hu et al. (2023)	Shanyutan wetland, Fujian, China	0–50 cm (marsh organ experiment)	*P. australis* (at marsh surface)	**Clay loam:** 12–14 **Sandy loam:** 8–9
			P. australis (20-cm below current marsh surface)	**Clay loam:** 14–16 **Sandy loam:** 11–13
			P. australis (40-cm below current marsh surface)	**Clay loam:** 18–19 **Sandy loam:** 12–14
Zhu et al. (2023)	Fuzhao wetland, Fujian, China	0–20 cm	*S. alterniflora*	14.15
Lin et al. (2023)	Minjiang, Zhanjiang, and Jiulong river estuary, China	0–10 cm	*S. alterniflora*	6–14
			K. obovata	11–15
Lin et al. (2023)	Beihai, Zhanjiang river estuary, Zhanjiang, China	0–10 cm	*S. alterniflora*	6–21
			A. marina	8–15
Wang et al. (2021)	Dongzhaigang mangrove, Hainan, China	0–10 cm	*Rhizophora sp.*	16.10
Dicen et al. (2019)	Masinloc, Palawan, Philippines	0–100 cm	*R. apiculata, R. stylosa*	25 ± 9
	Subic, Cebu, Philippines		*A. marina, S. alba, R. mucrolata, R. stylosa*	15 ± 9
	Bogtong, Zambales, Philippines			14 ± 4
	Calauit, Zambales, Philippines			11 ± 4
	Oboob, Cebu, Philippines			12 ± 2
	Kodia, Palawan, Philippines		*R. apiculata, R. stylosa*	10 ± 2

analyzer coupled to a Thermo Electron DeltaV Advantage isotope ratio mass spectrometer at Department of Geological Sciences, University of Florida. Prior to total organic carbon (TOC) and $^{13}C/^{12}C$ stable isotope measurement, soil samples were decarbonated by acid fumigation (Harris et al., 2001). Another set of unacidified samples was analyzed for total nitrogen (TN). Bulk elemental parameters and stable isotope ratios were quantified by comparing instrumental responses with L-glutamic acid laboratory standard (USGS40, USGS41). TOC of bulk soil (OC_{Bulk}) was reported as mass percentages of dry soil. C/N ratio was calculated from the molar ratio of TOC: TN. Stable isotope ratios were reported in $\delta^{13}C$ notation relative to Vienna Pee Dee Belemnite. Three to five replicates of 2 samples from the same depth of each core were measured for TOC, TN, and $\delta^{13}C$, their means and standard deviations were reported in Table S1. We also measured TOC, TN, and $\delta^{13}C$ in fresh and degraded leaf and root samples (total n = 54) from all plant types.

2.4. Separation of MAOC and POC

Separation of MAOM-POM was performed on soil samples from 2 cores for each plant community (total n = 96). The Cambardella and Elliott (1992) MAOM and POM separation protocol operationally defines MAOM as the fraction of soil organic matter with particle size smaller than 53 μm and higher density than 1.85 g cm^{-3}, while the lighter-and-larger fraction was defined as POM. However, a shortcut to separate MAOM-POM by particle size alone was suggested in a recent study (Cotrufo et al., 2019). This approach has been used in ca. 50 % of the previous studies that separate MAOM-POM in coastal wetland soils (Table 2; Feng et al., 2019; Fu et al., 2024; Ma et al., 2024; Sun et al., 2023; Zhang et al., 2024, 2021), as well as several studies of terrestrial soils (Chari and Taylor, 2022; Midwood et al., 2021; Patra et al., 2022; Rocci et al., 2022). One study performed density fractionation to validate size-alone method short-cut (Fu et al., 2024). They observed larger POM fraction based on size-alone method, yet both methods yielded similar MAOM concentration. In this study, we followed the Cotrufo et al. (2019) method to separate and define MAOM and POM by particle size alone, then performed density fractionation on four selected samples for validation (one per each plant type, number of replicates per sample = 3 or 10; see Text S1). We observed that elimination of the density fractionation step did not significantly alter the $\delta^{13}C$ values of the POC fraction (Lin's CCC = 0.99 ± 0.00); thus, this method short-cut did not affect the interpretation of $\delta^{13}C$ of each SOC sub-fraction (section 3.4 and 4.2). However, elimination of the density fractionation step resulted in a significant increase in %OC measured in the POM fraction (Lin's CCC = 0.11 to 0.55). This was probably due to the removal of OC-free heavy mineral grains (e.g., quartz sands with grain size > 53 μm, and density > 1.85 g cm^{-3}) which decreased the denominator of %OC

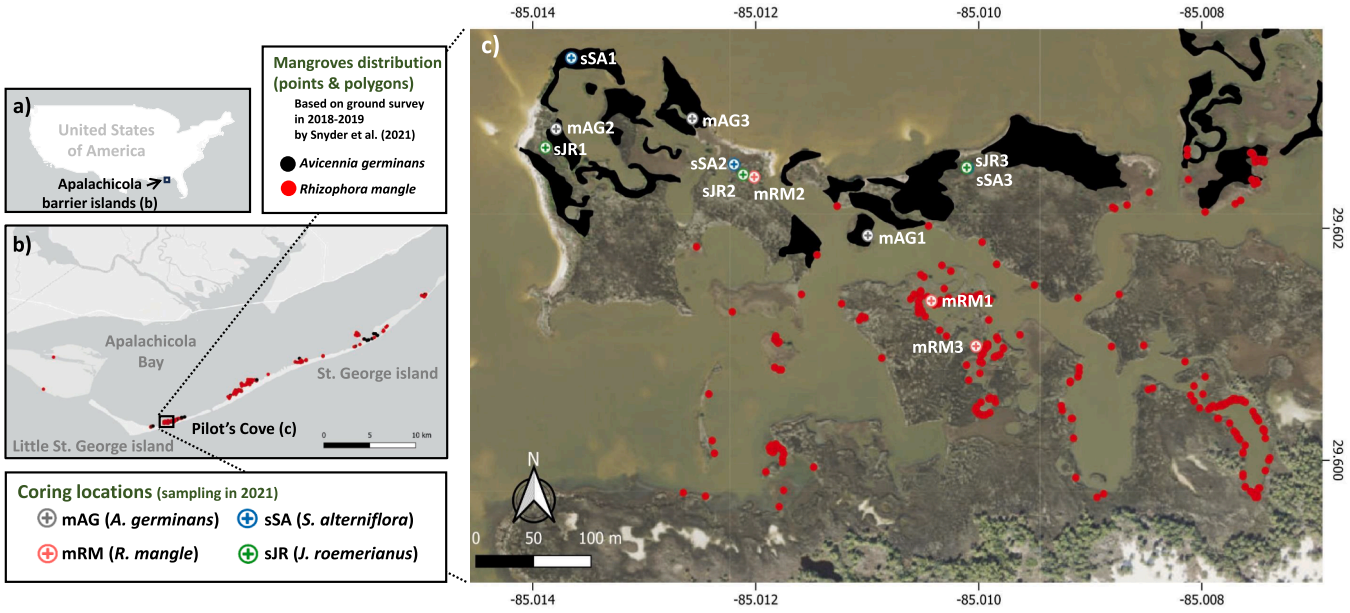

Fig. 1. Location of Apalachicola Estuary in the northern Gulf of Mexico (a). Mangrove distribution on Apalachicola Bay barrier islands (b). Mangrove distribution at Pilot's Cove, and our coring locations (c). All mangrove distribution data was reported in Snyder et al. (2021), based on 2018–2019 ground survey. The base maps were obtained from https://www.google.com/maps (accessed on 9/29/2021).

per dry soil mass. Therefore, we did not use the %OC measured in the POM fraction to represent POC content, but calculated POC content from the difference between bulk SOC and MAOC (Eq. 2; see next paragraphs). Hence, it is important to emphasize that our operationally defined POC may not represent the actual amount of plant detritus in soils. The comparison of our estimates to previous works needs to consider the large inconsistency in size and/or density fractionation scheme (see reviews in Table 2). Further information on this method validation can be found in Text S1.

Size-separation was performed by shaking homogenized soil samples in 0.5 g/L sodium hexametaphosphate solution for ~ 15 h to completely break down soil aggregates, then filtering through a 53-μm sieve. The fraction that passed through the 53-μm sieve was rinsed with Milli-Q water and collected as MAOM, while the materials retained on the sieve were rinsed with Milli-Q water and collected as POM. We did not use artificial seawater solution to rinse either of the size fractions, in an attempt to avoid any possible dissolution of weakly bound MAOM that may occur in high ionic strength seawater (Text S2). Both fractions were freeze-dried and weighed. The fraction of fine-grained (<53 μm) particles (%fine fraction) was calculated by dividing the dry mass of soil particles that pass through 53-μm sieve by dry mass of bulk soil sample and multiplied by 100. Organic carbon, TN, and $\delta^{13}C$ were measured in MAOM and POM fractions following the method in section 2.3.

The recovery of soil mass from POM-MAOM separation was 81.1 ± 14.6 %. The loss of soil mass was probably due to 1) the dissolution of water-soluble components (both water-extractable OC and soluble inorganic soil minerals) (e.g., Wardinski et al., 2022; see Text S2 for more details), and 2) the removal of shell fragments from POM fraction by hand during the wet sieving process. We selectively removed shell materials because their incomplete dissolution during acid fumigation could generate inorganic carbon residuals in the POM fraction, which would potentially lead to overestimation of POC and interfere with the measurement of $\delta^{13}C$ in the POM fraction. Therefore, we decided not to use mass recovery of POM fraction to calculate POC (see Text S2 for more details). MAOC content (gram of OC per 100 g of bulk soil dry mass) was calculated from the measured OC% in the < 53-μm fraction as the mass percentage relative to dry soil mass. The fraction of bulk SOC, classified as MAOC (f_{MAOC}), was calculated by dividing OC in MAOC by OC_{Bulk} (Eq. 1) (Rocci et al., 2022), since the combination of POC and MAOC is theoretically equal to OC_{Bulk}, POC was calculated by subtracting MAOC from OC_{Bulk}, while f_{POC} was derived from subtracting f_{MAOC} from 1 (Eq. 2). Full discussion on the artifacts of this calculation is in Text S2.

$$f_{MAOC} = MAOC/OC_{Bulk} \quad (1)$$

$$f_{POC} = 1 - f_{MAOC} \quad (2)$$

2.5. Separation of FeR-MAOC

Concentrations of FeR and FeR-MAOC were determined by the citrate-bicarbonate-dithionite (CBD) reduction method (Lalonde et al., 2012). We used bulk soil samples, not the MAOM fraction, as a primary substrate for CBD treatments to maintain the consistency of the method used in the literature, and to avoid the artifacts of sodium hexametaphosphate which can affect the recovery and composition of FeR-MAOC, as observed in our method validation test (Text S3). Prior to CBD reduction, a control experiment was performed to correct for the loss of OC due to CBD treatment conditions (e.g., ionic strength, temperature) – not related to reductive dissolution of the reactive iron (hydr)oxide minerals. Briefly, bulk soil samples were extracted with sodium chloride (NaCl) and sodium bicarbonate ($NaHCO_3$) solution. The mixture was heated, cooled down, and centrifuged to separate supernatant solution from the residual solids. The solids were freeze-dried. A sub-sample was analyzed for TOC and $\delta^{13}C$ (defined as $OC_{Control}$ and $\delta^{13}C_{Control}$), following the method described in section 2.3. The remaining solids were treated with trisodium citrate-$NaHCO_3$ solution, and sodium dithionite (a.k.a. CBD treatment) to solubilize FeR-MAOC. After the experiment, post-CBD supernatant solutions were separated from the post-CBD solids. The post-CBD solid residue was freeze-dried and analyzed for TOC and $\delta^{13}C$ (defined as OC_{CBD} and $\delta^{13}C_{CBD}$). The fraction (%) of OC associated with FeR ($f_{FeR\text{-}MAOC}$) in bulk SOC (OC_{Bulk}) was calculated using Eq. 3. FeR-MAOC and nonFeR-MAOC were reported as grams of OC per 100 g of dry soil mass.

$$f_{FeR-MAOC} = \frac{OC_{Control} - OC_{CBD}}{OC_{Bulk}} \times 100 \quad (3)$$

The fraction of OC associated with other minerals, insensitive to the CBD reduction method ($f_{nonFeR\text{-}MAOC}$), which includes but is not limited to clay-bound OC, was calculated from the difference between f_{MAOC} and $f_{FeR\text{-}MAOC}$ (Eq. 4):

$$f_{nonFeR-MAOC} = f_{MAOC} - f_{FeR-MAOC} \quad (4)$$

A select number of post-CBD supernatant solutions (n = 84), from both control- and CBD-treatment, were analyzed for dissolved iron content by an Element 2 HR-ICP-MS. The concentration of extractable FeR (μmol Fe per g soil) was calculated from the difference between dissolved iron in the post-control and post-CBD supernatant solutions.

While FeR-MAOC values derived from the CBD method are widely accepted in the literature, recent work has suggested that the NaCl solution used in the control experiment could liberate up to ~ 44 % of FeR-MAOC (Fisher et al., 2020). Hence, Fisher et al. (2020) suggested that the 'control experiment' be omitted, and that FeR-MAOC be estimated by the difference between OC_{Bulk} and OC_{CBD} (Eq. S2). Here, while our FeR-MAOC results were reported following the classical CBD method (Lalonde et al., 2012), we used the Fisher et al. (2020) approach to calculate for the maximum FeR-MAOC (FeR-$MAOC_{max}$) and minimum nonFeR-MAOC (nonFeR-$MAOC_{min}$) values (Text S4).

We calculated the offset between $\delta^{13}C$ of bulk SOC and each of its sub-fractions (POC and MAOC), following Eq. 5. For FeR-MAOC, the isotopic mass balance equation (Huang et al., 2021) was not used to calculate $\delta^{13}C_{FeR\text{-}MAOC}$ due to the significant loss of OC during control experiment (Text S5). Instead, we calculated $\delta^{13}C_{Offset}$ CBD-Bulk, which is the difference between $\delta^{13}C$ of bulk soil and $\delta^{13}C$ of post-CBD solid residuals.

$$\delta^{13}C_{Offset}X \leftrightarrow Bulk = \delta^{13}C_X - \delta^{13}C_{BulkSOC} \quad (5)$$

where, $\delta^{13}C_{Offset}$ X-Bulk represents the difference between $\delta^{13}C$ measured in fraction X (POC, MAOC, and post-CBD solid residues) and $\delta^{13}C$ measured in bulk SOC. The interpretation of positive and negative values of each $\delta^{13}C_{Offset}$ is summarized in Table S6. The content and $\delta^{13}C$ of POC, MAOC, and FeR-MAOC were analyzed in 3 replicates of 8 selected samples, their averaged values and standard deviations were reported in Table S7.

2.6. Mössbauer spectroscopy

Mössbauer spectroscopy distinguishes Fe-bearing mineral phases and Fe oxidation states, and determines the quantitative distribution of Fe between mineral phases and oxidation states (Gütlich et al., 2012; Gütlich and Schröder, 2012). Mössbauer spectra were acquired from a select subset of samples from one core per plant habitat (mAG1, mRM1, sSA2, sJR3; n = 2 to 3 per core), using a miniaturized Mössbauer spectrometer MIMOS II (Klingelhöfer et al., 2003). The 14.4 keV gamma-radiation source was Co-57 in Rh matrix and was kept in constant acceleration mode (triangular waveform). All samples were measured in backscattering geometry in plastic bags at room temperature, and spectra were calibrated against a spectrum of alpha-iron foil (25 um thickness) – also at room temperature. Spectra were evaluated using Lorentzian line shapes with an in-house software routine (Mbfit) based on the least-squares minimization routine MINUIT (James, 2004); no f-factor correction was applied.

2.7. Radionuclide dating

One soil core from each plant habitat type (mAG1, mRM1, sSA2, sJR3) was selected for radionuclide-based dating to compare rates of sediment accumulation in recent decades. The detailed method for radionuclide measurement is described in Smoak et al. (2013) and Breithaupt et al. (2014). Briefly, gamma activities were counted with an intrinsic germanium well detector and multichannel analyzer. Activity of ^{210}Pb was measured with the 46.5 keV peak; ^{226}Ra activity was measured using its proxy ^{214}Pb (351.9 keV peak) (Appleby et al., 1988), and ^{137}Cs was measured by the 661.7 keV peak. Soil age-depth models were reconstructed using excess ^{210}Pb and the Constant Initial Concentration (CIC) dating model (Appleby and Oldfield, 1992) which can be applied to partial linear segments of the depth profile of the natural log of excess ^{210}Pb. Although multiple CIC fits can be applied to a single core profile, this should be avoided if slope changes are not monotonic with depth as this can indicate a violation of model assumptions about the source and consistency of the concentration in surface sediments at the time of introduction. When ^{137}Cs was detected (Drexler et al., 2018), the peak of activity was assumed to represent the year 1963 and was compared with the ^{210}Pb age estimation. Soil mass accumulation rates (g m^{-2} $year^{-1}$) were calculated by dividing cumulative mass per unit area (g m^{-2}) of a given depth interval by the number of years represented by that interval. Organic C burial rates (g m^{-2} $year^{-1}$) were determined by multiplying mass accumulation rate by OC_{Bulk}.

2.8. Statistical analyses

Statistical analyses were performed using R 4.2.3 (R Development Core Team, 2023). The normality assumption was first verified by the Shapiro-Wilk test. Since most of the data were not normally distributed, we used Kruskal-Wallis test (non-parametric Analysis of Variance), followed by Dunn's test, to determine the influence of plant species on each SOC sub-fraction. The statistical differences between $\delta^{13}C$ of bulk SOC and $\delta^{13}C$ of each SOC sub-fraction were compared using a two-sided *t*-test. Pearson's correlation was used to describe downcore trends of a single parameter with depth. When the number of samples was too small (n < 30), we used Bootstrapping statistics (package "boot" in R; Canty and Ripley, 2022) to resample data from a single data set 10,000 times before performing aforementioned statistical tests. The results of Kruskal-Wallis test, *t*-test, and Pearson's correlation were reported in the format of "χ^2/ t(d.f.)/ r(d.f.) = [Chi-square/ t-statistics/ Pearson's r respectively], p = [p-value]".

3. Results

3.1. Soil physical properties, reactive iron, and soil mass accumulation

Living roots were visible throughout the cores, to a depth of ca. 45 cm, in all habitat types. *R. mangle* soil cores had more reddish color (likely from both Fe-staining and/or accumulation of tannins) than all cores from the other plant habitats. The percent fine fraction (<53 μm) was generally higher and less variable in mangrove than salt marsh soils (Fig. S1, Table 4, S8). The concentration of FeR released from the CBD treatment was significantly higher ($\chi^2 = 30.67$, p = 0.002) in the top 22 cm of both *R. mangle* cores (median = 292.8 ± 48.0 μmol Fe per mg soil) (Fig. 2), compared to soils from *A. germinans*, *S. alterniflora* and *J. roemerianus* habitats (median = 34.2 ± 25.7 μmol Fe per mg soil).

Mössbauer Spectra of the *A. germinans* core showed large center shift δ and quadrupole splitting Δ_{EQ} values (Fig. S2, Table S9). This probably indicates (super)paramagnetic high-spin Fe(III) (hydr)oxides, such as the CBD extractable reactive iron phases ferrihydrite, lepidocrocite, goethite and hematite (Vandenberghe and De Grave, 2012), coexisted with pyrite. In contrast, two iron phases were observed in the Mössbauer Spectra of the *R. mangle* core. Larger δ and Δ_{EQ} values in samples, from soil depths 6 and 16-cm, indicated the predominance of (super)paramagnetic iron (hydr)oxides over pyrite, which was consistent with the largest amount of CBD extractable iron and the red coloration in the upper section of core mRM1. A second Fe phase [Fe(II)], likely in a clay mineral, increased with depth in the core mRM1, indicative of reducing conditions. This was also reflected in the parameters of the more abundant phase where both δ and Δ_{EQ} values were lower in the sample from 36-cm depth, indicating higher abundance of pyrite with increasing depth.

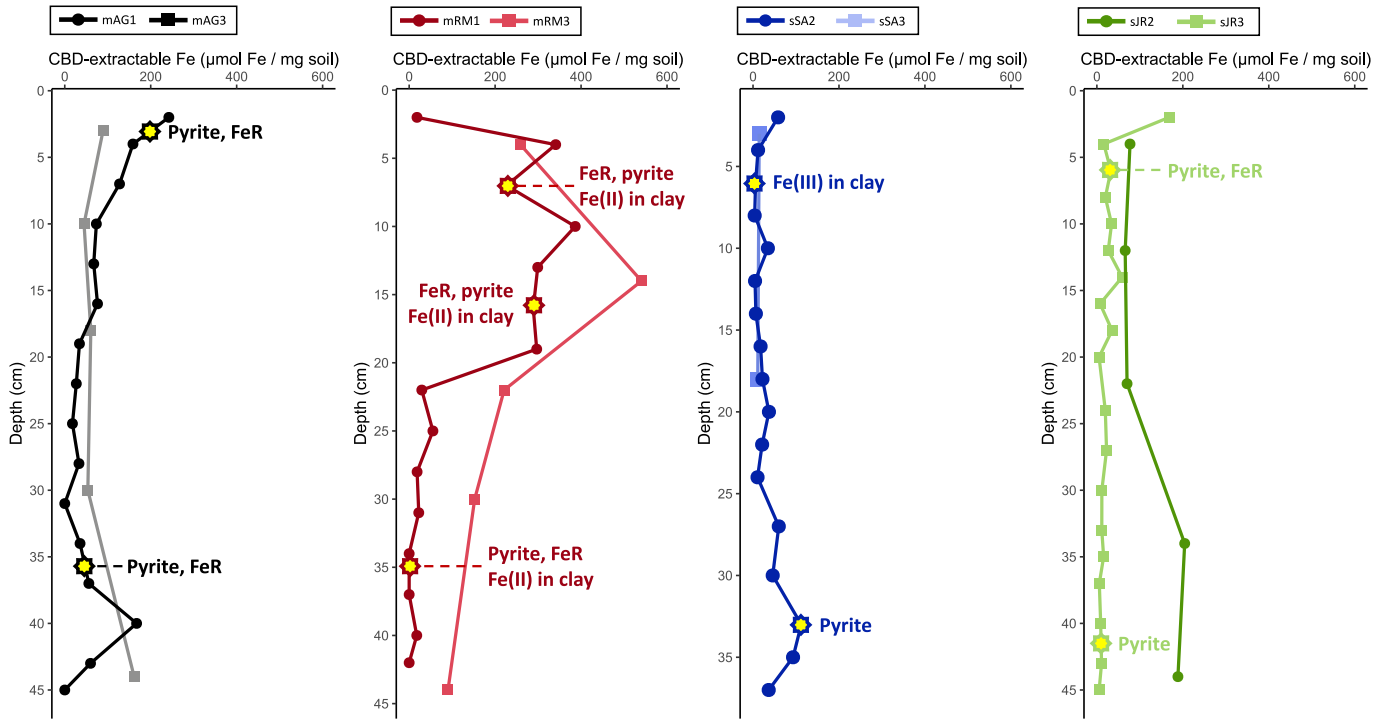

Fig. 2. Variation in iron speciation and mineralogy across soil cores and depths. The line graphs and solid-filled data points represent downcore variation in CBD-extractable iron concentrations, while stars represent samples that were analyzed by Mössbauer spectroscopy for Fe-bearing mineral phases.

The spectra of both salt marsh soil cores each showed a single iron phase in each depth. The Mössbauer parameters for the bottom layers of both salt marsh soils and the top layer of the *J. roemerianus* core indicated the diamagnetic low-spin Fe(II) mineral pyrite (Vandenberghe and De Grave, 2012). The top layer of the *S. alterniflora* core had Fe(III) in tetrahedral coordination indicated by the low center shift δ and quadrupole splitting Δ_{EQ} values, which could be Fe substituting for Si in a clay mineral; consistent with the low amounts of CBD extractable iron from these cores.

Excess ^{210}Pb depth profiles varied considerably among the four cores. While core mRM1 and sJR3 showed an overall linear decline in ln (excess ^{210}Pb) down to the bottom of the core (R^2 = 0.94 and 0.90 respectively), the other core profiles (mAG1, sSA2) suggest changes in sedimentation rates and/or vertical mixing (Fig. S3). The highest mass accumulation rate was observed in core mRM1, followed by core sJR3 and mAG1 respectively (Table 4). In contrast, core sSA2 had a uniquely low mass accumulation rate in the shallow section. According to the age-depth models (Fig. S3), the soil depths at 16.7 and 10.7 cm, in cores mAG1 and mRM1, were deposited when *A. germinans* (1986) and *R. mangle* (2008) were firstly observed on Little St. George Island, respectively (Snyder et al., 2021).

3.2. Bulk SOC and its $\delta^{13}C$ composition

Bulk SOC from *A. germinans*, *R. mangle*, *S. alterniflora*, and *J. roemerianus* plant habitats was independent of plant habitat type and negatively correlated with soil depth ($r(284) = -0.51$, $p < 0.001$) (Fig. 3). All mangrove soil cores showed gradual decreases in OC_{Bulk} with depth (Fig. 3a, 3b). Conversely, OC_{Bulk} of salt marsh soils showed more variable trends with depth (Fig. 3c, 3d). Across all plant habitats, SOC stock was slightly lower in mangrove habitats compared to salt marshes (Table 4). OC burial rates, on the other hand, were conspicuously lower in salt marsh habitats, especially *S. alterniflora* relative to the mangroves (Table 4).

Table 4
Properties of bulk soil and bulk SOC. For mass accumulation rate, accretion rate, and OC burial rate, the number in square brackets represents time intervals that the constant rates were reported (see Fig. S3 for more details). For OC stock, the numbers in square brackets represent depth intervals.

Parameters	Plant habitats			
	A. germinans	*R. mangle*	*S. alterniflora*	*J. roemerianus*
Soil physical properties				
%fine fraction (<53 μm)	61.4 ± 9.4	58.1 ± 9.4	23.5 ± 28.9	34.2 ± 14.0
CBD-extractable reactive iron (μmol Fe / mg sediment)	59.9 ± 27.4	292.8 ± 48.0 (Top 22 cm)	21.2 ± 15.3	21.1 ± 24.6
Soil and OC accumulation based on radionuclide dating				
Representative core	mAG1	mRM1	sSA2	sJR3
Mass accumulation rate ($g\ m^{-2}\ yr^{-1}$)	1372.2 ± 160.8 [45 ± 5 years]	3298.8 ± 180.6 [52 ± 3 years]	318.0 ± 134.8 [88 ± 26 years]	1590.3 ± 93.9 [114 ± 7 years]
Accretion rate ($mm\ yr^{-1}$)	4.7 ± 0.5 [45 ± 5 years]	8.1 ± 0.4 [52 ± 3 years]	1.1 ± 0.2 [88 ± 26 years]	2.8 ± 0.2 [114 ± 7 years]
OC burial rate ($g\ m^{-2}\ yr^{-1}$)	124.6 ± 14.7 [45 ± 5 years]	208.4 ± 13.0 [52 ± 3 years]	42.2 ± 18.0 [88 ± 26 years]	107.5 ± 12.8 [114 ± 7 years]
OC stock ($kg\ m^{-2}$)	2.66 [0–10 cm] 11.25 [0–45 cm]	2.76 [0–10 cm] 10.83 [0–42 cm]	3.72 [0–10 cm] 12.32 [0–37 cm]	3.72 [0–10 cm] 12.23 [0–32 cm]

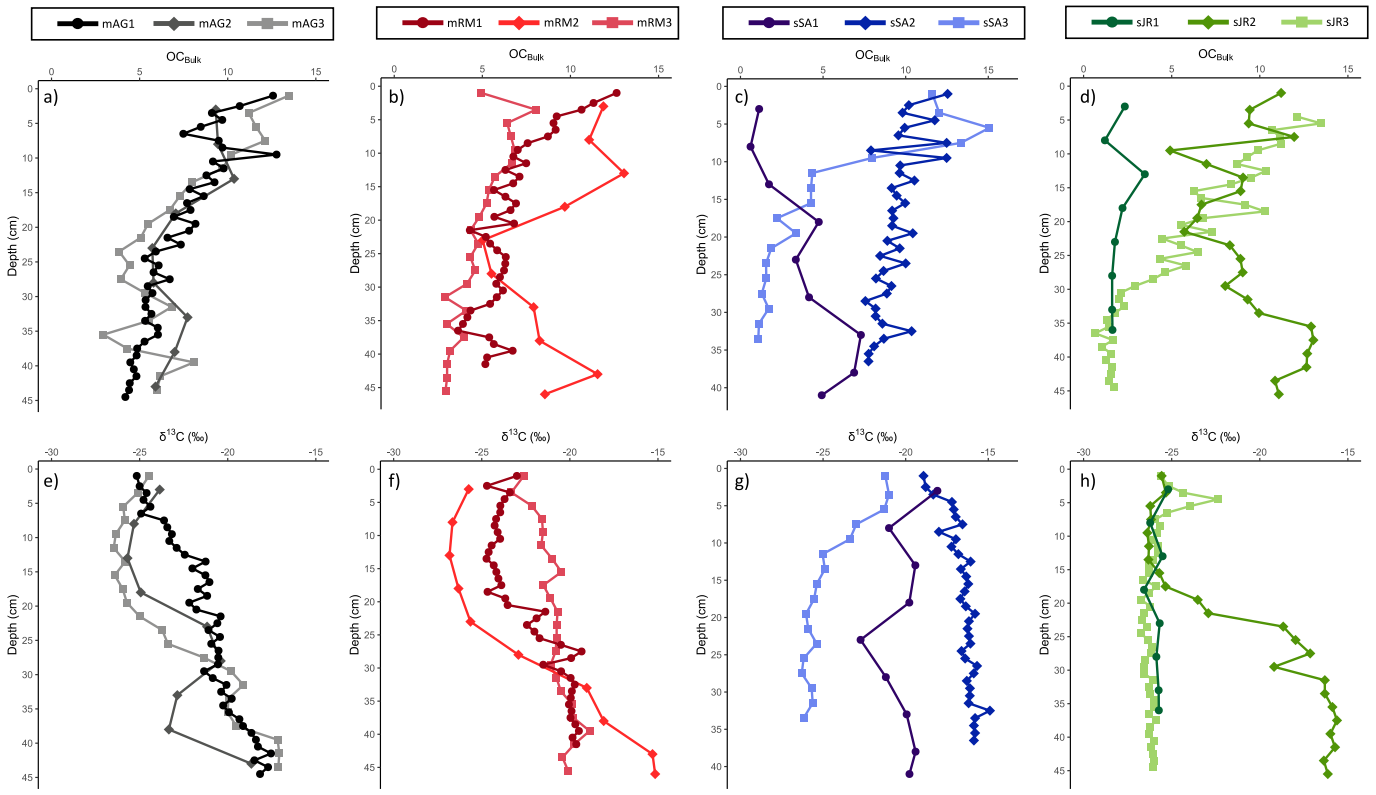

Fig. 3. OC_{Bulk} and bulk $\delta^{13}C$-depth profiles of *A. germinans* (a, e), *R. mangle* (b, f), *S. alterniflora* (c, g), and *J. roemerianus* soil cores (d, h).

The analysis of $\delta^{13}C$ in fresh leaves, stems, and roots of plant endmembers revealed that C_3 plants were distinctively more depleted in $\delta^{13}C$ (*A. germinans*, *R. mangle*, and *J. roemerianus*, median = -26.8, −28.1, and −26.4 ‰ respectively) than C_4 *S. alterniflora* salt marsh (median = -13.6 ‰) ($\chi^2 = 17.5$, n = 28, $p < 0.0001$) (Fig. S4). The $\delta^{13}C$ in bulk soil samples ranged between C_3 and C_4 plant endmembers and varied with depth and across plant habitats. All mangrove soil cores showed a unidirectional up-core depletion of $\delta^{13}C$ (Fig. 3e, 3f). In contrast, the $\delta^{13}C$-depth profiles for each replicate salt marsh score were different from one another (Fig. 3g, 3h). Further interpretation of each $\delta^{13}C$ profile can be found in section 4.1.

3.3. POC, MAOC, and FeR-MAOC content

Soils from *A. germinans* and *R. mangle* mangrove habitats contained a larger fraction of MAOC compared to POC ($t(49) = 3.96$, $p < 0.001$). The average POC and MAOC content in mangrove soils were 2.00 ± 0.78 and 3.77 ± 0.77 g per 100 g dry soil, which equated to 38.39 ± 6.01 % and 61.61 ± 6.01 % of total SOC, respectively (Table 2, Fig. 4). In contrast, POC was greater than MAOC in both *S. alterniflora* and *J. roemerianus* salt marshes ($t(47) = 7.89$, $p < 0.001$). The average POC and MAOC content in salt marsh soils were 4.20 ± 1.64 and 3.52 ± 1.87 g per 100 g dry soil, representing 58.77 ± 9.02 % and 41.23 ± 9.02 % of total SOC, respectively. While POC content of most soil cores was negatively correlated with depth, there were no distinctive trends with the %fine fraction. In contrast, MAOC in most soil cores decreased with depth and increased with the increasing %fine fraction (Table S10).

To determine differences in POC, MAOC, and FeR-MAOC content across plant habitats, a Kruskal-Wallis test was performed on integrated data from all cores and all depths. We also separately performed Kruskal-Wallis test on each group of soil samples from shallow soil (0–15 cm depth), middle soil (15–30 cm depth), and deep soil (30–45 cm depth) sections. Box plots, Chi-squares, and p-values for each relationship are reported in Fig. 5 (after sandy outliers [%fine fraction < 20 %] were excluded) and S5 (included all data points). All sandy outliers were removed from the dataset because 1) the quantification of their %OC was highly variable due to the heterogenous distribution of fine OC-rich particles within the pores of coarse OC-free sand clasts; and 2) their OC_{Bulk} was extremely low (~0.5 %), as were POC, MAOC, and FeR-MAOC content, leading to a bimodal data distribution in the box plots, especially in the middle and deep soil sections (Fig. S5).

Across the entire data set, POC content was significantly higher in salt marsh habitats compared to mangroves (Fig. 5). In the shallow and middle soil sections, *R. mangle* was the only mangrove habitat that had significantly lower POC content than salt marshes. In contrast, both *A. germinans* and *R. mangle* mangrove soils contained less POC than salt marshes in the deep soil section (Fig. 5). MAOC content, on the other hand, was overall independent of plant taxa. While there was no statistical differences in MAOC content among all plant habitats in shallow soil section, *S. alterniflora* habitat contained slightly higher MAOC than other plants in the middle soil section. Both *S. alterniflora* and *J. roemerianus* salt marsh habitats had larger MAOC content than those of *R. mangle* in the deep soil section. The f_{POC} was overall higher in salt marsh than mangrove habitats (Fig. S6) and the f_{MAOC} was significantly higher in mangroves than salt marshes.

FeR-MAOC represented a minor fraction of the coastal wetland soils on Apalachicola barrier islands; the average $f_{FeR\text{-}MAOC}$ of the entire data set was 6.61 ± 6.62 % of SOC, which was equal to 0.54 ± 0.62 g of FeR-MAOC per 100 g dry soil (Fig. 4). Across all plant habitats, FeR-MAOC values represented a smaller fraction of total MAOC (13.74 ± 15.55 % of total MAOC) compared to nonFeR-MAOC. Interestingly, *R. mangle* soils had lower FeR-MAOC content and $f_{FeR\text{-}MAOC}$ than all other plant habitats (Fig. 5, S5, S6). While this relationship was prominent in shallow soils, the difference in FeR-MAOC between *R. mangle* and other plant habitats became smaller in the middle and deep soil sections because the FeR-MAOC content of the 3 other plant habitats decreased with depth. The maximum amount of FeR-MAOC that could possibly exist in our soil samples ($FeR\text{-}MAOC_{max}$) was 1.18 ± 1.30 g per 100 g dry

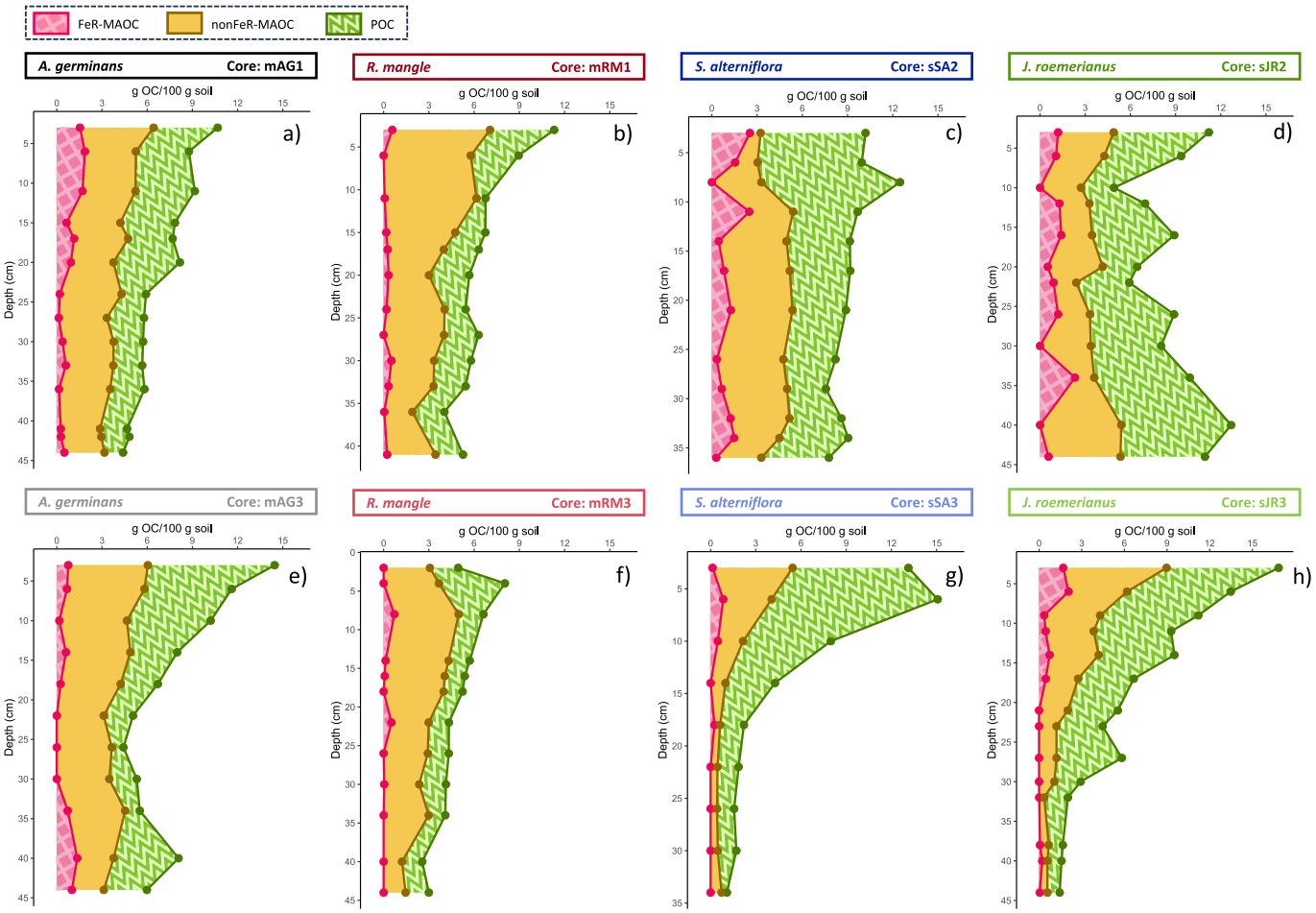

Fig. 4. Partitioning of bulk SOC into POC, FeR-MAOC, and nonFeR-MAOC fraction of each soil core.

soil (14.83 ± 12.53 % of SOC) (Fig. S7), yet the concentration of FeR-MAOC$_{max}$ was still smallest in *R. mangle* habitats relative to the 3 other plant communities ($\chi^2 = 14.2$, p = 0.03).

3.4. Composition of bulk SOC, POC, MAOC, and FeR-MAOC

Across all soil cores and depths, the C/N ratio of POC fraction was generally greater than C/N of bulk SOC (t = 2.28 to 8.65; p = < 0.001 to 0.003), except core sSA3 which shows no statistical difference (Fig. 6). In contrast, the molar C/N ratio of MAOC was significantly lower than bulk SOC (t = 3.04 to 4.84; p = < 0.001 to 0.009), except for cores mAG3 and sJR2, which showed no statistical difference.

While the downcore variation of δ^{13}C of POC, MAOC, and FeR-MAOC resembled the pattern of δ^{13}C-bulk SOC (Fig. S8), the offset between δ^{13}C of bulk SOC and each sub-fractions varied significantly across plant types and soil depths (Fig. 7); see t-statistics and p-value of each $\delta^{13}C_{offset}$, separated by soil sections (shallow, middle, and deep) in Table S11. The interpretation of positive and negative $\delta^{13}C_{offsets}$ can be found in Fig. 7 and Table S6. The shallow sections of soil cores from C_3 plant habitats (*A. germinans*, *R. mangle*, and *J. roemerianus*) were dominated by a negative $\delta^{13}C_{offset}$ POC-Bulk (Fig. 7a, 7d). The largest difference between δ^{13}C-POC and bulk SOC was observed in *R. mangle* habitats, where δ^{13}C values of POC were less than bulk SOC by as much as −5.35 ‰ (Fig. S8). In contrast, δ^{13}C values of POC were generally greater than bulk SOC in C_4 plant habitats (*S. alterniflora*), especially in the middle and deep soil sections of core sSA2 that yielded the maximum $\delta^{13}C_{offset}$ POC-Bulk at +1.97 ‰. The $\delta^{13}C_{offset}$ POC-Bulk gradually decreased with depth and converged to zero (Fig. 7a, 7d), especially in cores that exhibited distinctive down-core variation in δ^{13}C-SOC (all mangrove cores, and sJR2) (Fig. 3). The $\delta^{13}C_{offset}$ MAOC-Bulk in shallow soils of C_3 mangroves and *J. roemerianus* habitats was significantly positive (up to + 2.78 ‰ in *A. germinans* habitats), followed by a gradual decrease with depth (Fig. 7b, 7e). Conversely, both C_4 *S. alterniflora* cores had negative $\delta^{13}C_{offset}$ MAOC-Bulk throughout the entire core, without a strong relationship with depth.

The $\delta^{13}C_{offset}$ CBD-Bulk was mostly positive in shallow soils of C_3 plant habitats (*A. germinans*, *R. mangle*, and *J. roemerianus*), with a maximum offset at +0.51 ‰ in core mAG1. In contrast, $\delta^{13}C_{offset}$ CBD-Bulk was mostly negative in C_4 *S. alterniflora* habitats (Fig. 7c, 7f). According to the interpretation guideline in Table S6, this pattern emphasized that FeR-MAOC was more δ^{13}C-depleted than OC_{Bulk} in C_3 plant habitats, while it was more δ^{13}C-enriched than OC_{Bulk} in C_4 plant habitats. The difference between $\delta^{13}C_{CBD}$ and $\delta^{13}C_{Bulk}$ declined with depth until they were not statistically different in the deep soil section of all cores.

4. Discussion

4.1. Changes in bulk SOC sources and formation mechanisms following mangrove-salt marsh replacement

The seeming paradox of elevated organic carbon burial rates in mangrove environments alongside greater organic carbon stocks in salt marshes underscores distinct mechanisms of organic carbon formation between mangrove and salt marsh habitats. The correlation between high mass accumulation rate and high OC burial rate in the top 10-cm of mangrove soil cores suggests that SOC accumulation in mangrove habitats was principally driven by particle deposition. Mangroves are in

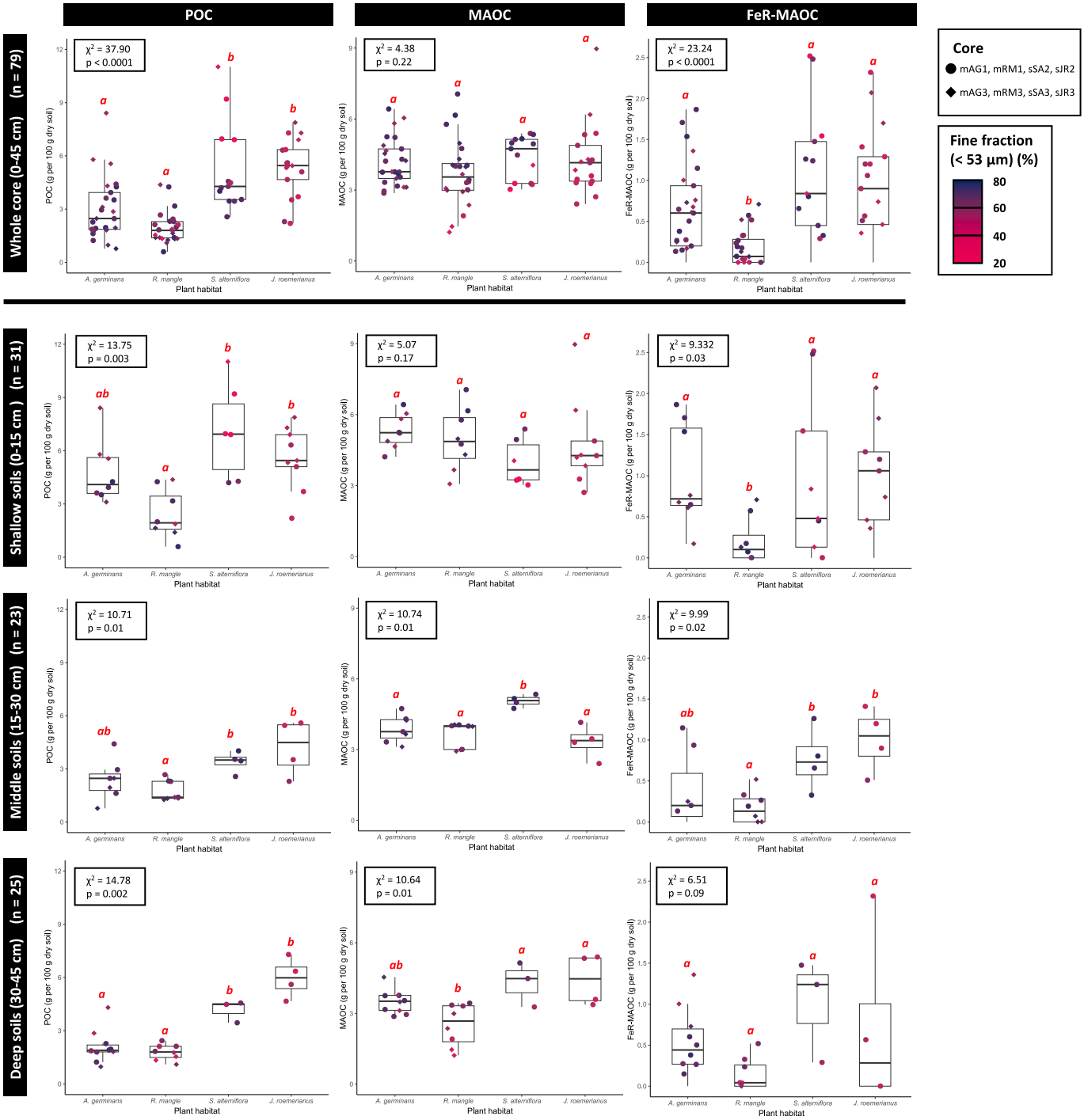

Fig. 5. Box plots of POC, MAOC, FeR-MAOC content in all soil samples, soil samples from shallow, middle, and deep soil sections classified by plant habitats. This figure only displays the data points with < 20 % fine fraction. The lower and upper hinges indicate the first and third quartiles. The upper and lower whiskers cover data points within 1.5 × interquartile range. Italic lowercase letters over each box plot group the data by statistical difference (Dunn's test, $p < 0.05$). The Chi-square and p-value of Kruskal-Wallis test were reported at the top left corner of each plot. The color of the jitter points represents %fine fraction of the soil depths where those data points came from.

areas of high sedimentation, notably due to their aerial roots (Furukawa and Wolanski, 1996; Willemsen et al., 2016), potentially leading to greater OC burial (Bianchi et al., 2013). A study comparing sediment deposition between mangrove taxa revealed that the prop roots of *R. mangle* can enhance sediment deposition better than the pneumatophores of *Sonneratia alba*, similar to those of *A. germinans* (Krauss et al., 2003). Enhanced trapping of fine particles in *R. mangle* habitats was reported to promote interactions between OC and mineral phases, resulting in higher OC burial (Jimenez et al., 2021). This may explain the higher mass accumulation and OC burial rates observed in the *R. mangle* soil cores compared to all other plant habitats (Table 4). On the other hand, salt marsh habitats have higher OC stocks than *R. mangle* despite their lower mass accumulation rate (Table 4). This suggests that OC in salt marsh soils largely originated from belowground processes (e.g., root biomass and rhizodeposits), which are independent of inorganic soil mineral sedimentation (Nyman et al., 2006). These findings are in

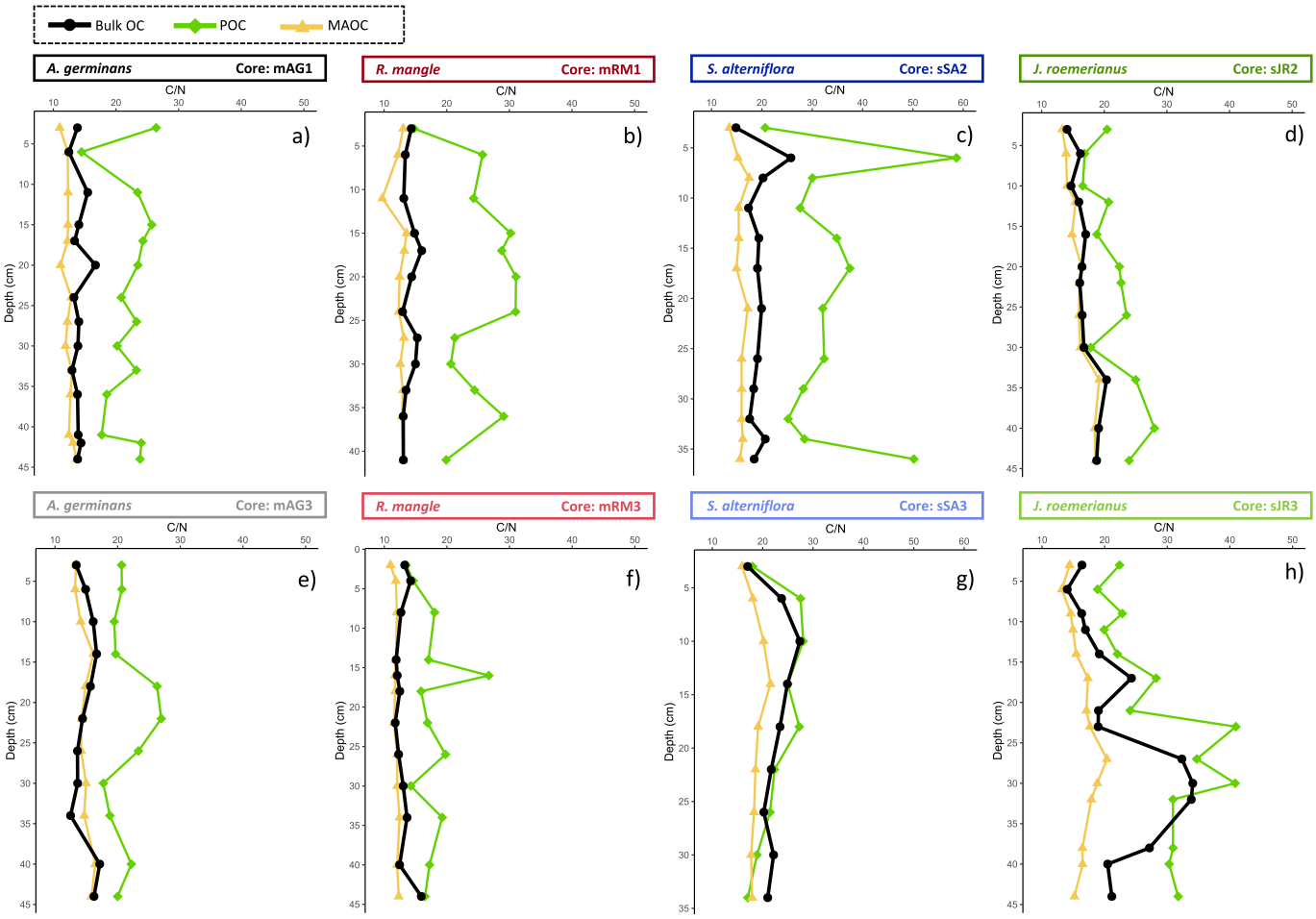

Fig. 6. Downcore variation in C/N ratio of bulk soil, POM, and MAOM fraction of each soil core.

agreement with the previous work which showed greater contributions of roots to OC burial in salt marshes than mangroves, largely due to slower decomposition rate of salt marsh roots than mangroves (Ouyang et al., 2017). Accumulation of root-derived OC was more enhanced in mature salt marshes compared to juvenile mangroves (more detail on section 4.2.1). It is important to note that the proposed mechanisms may differ across different regions since geomorphic factors typically dominate over plant-centric drivers (Breithaupt and Steinmuller, 2022). Nevertheless, these inherent plant effects are "pieces to the puzzle" that still remain largely ignored.

Down-core profiles of bulk soil $\delta^{13}C$ reveal a history of salt marsh replacement by mangroves and salt marsh-to-salt marsh transitions over the past ca. 50 years. In all mangrove cores, the up-core depletion of $\delta^{13}C$ (Fig. 3e, 3f) suggests a gradual replacement of C_4 *S. alterniflora* salt marshes by C_3 *A. germinans* and *R. mangle* mangroves. This succession may or may not include the intermediate phase of *S. alterniflora* transition to *J. roemerianus* before transitioning to mangroves. Although the replacement of *J. roemerianus* by mangroves is frequently observed in the field, the presence of intermediate *J. roemerianus* phase in soil cores needs further confirmation with source-specific proxies. Although Apalachicola barrier islands have experienced multiple periods of mangrove habitat expansion and contraction (Snyder et al., 2021), we did not observe alternating mangrove-salt marsh transitions in the soil $\delta^{13}C$ record. Instead, bulk $\delta^{13}C$ continuously increased from the top to the bottom of every soil core, without any abrupt shift in soil layers that were dated back to the first record of mangroves in this region (16.7 cm-depth of core mAG1 and 10.7 cm-depth of core mRM1; Fig. S3). This suggests contributions of mangrove-OC to subsurface soils, via root production (e.g., Arnaud et al., 2023) and/or rhizodeposition (e.g., Villarino et al., 2021). Nevertheless, further evidence is required to quantify the relative importance of leaf versus root-derived OC in SOC formation and OC burial.

Unlike the unidirectional global-warming-induced replacement of *S. alterniflora* by mangroves observed in all Apalachicola mangrove soil cores, soil cores from salt marsh habitats recorded the complex evolution of salt marsh-to-salt marsh transitions, between *S. alterniflora* and *J. roemerianus*. Some salt marsh soil cores showed no vegetation shift (sJR1, sJR3, sSA1, sSA2) while the others illustrated reciprocal substitution between *S. alterniflora* and *J. roemerianus* (Fig. 3g, 3h). The replacement of *J. roemerianus* by *S. alterniflora* was observed in core sSA3, according to up-core enrichment of $\delta^{13}C_{SOC}$. Since *S. alterniflora* commonly dominates over *J. roemerianus* in saline soils at low elevation (Sánchez, 2010; Touchette et al., 2009), transformation of *J. roemerianus* habitats to *S. alterniflora* might reflect regional sea level rise. This plant replacement may alternatively result from soil elevation loss due to hurricane damage, as observed at Pilot's Cove during Hurricane Michael in 2018 (Steinmuller et al., 2022a). On the other hand, up-core depletion of $\delta^{13}C_{SOC}$ in core sJR2 suggested the replacement of *S. alterniflora* by *J. roemerianus*, probably through a gain in elevation. Changes in elevation may be driven by increasing sediment deposition due to higher sediment load from Apalachicola River basin (Chen et al., 2014; Hovenga et al., 2016). Based on the higher abundance of coarse-grained sands in the salt marsh soil cores, elevation gain may also result from deposition of tidally-induced marine sands, or sediment trapping within the complex root systems of salt marshes.

Apart from vegetation replacement, the depletion of bulk SOC $\delta^{13}C$ in the shallow *R. mangle* soil section may partially result from accumulation of *R. mangle* leaves, which are more $\delta^{13}C$-depleted than *R. mangle*

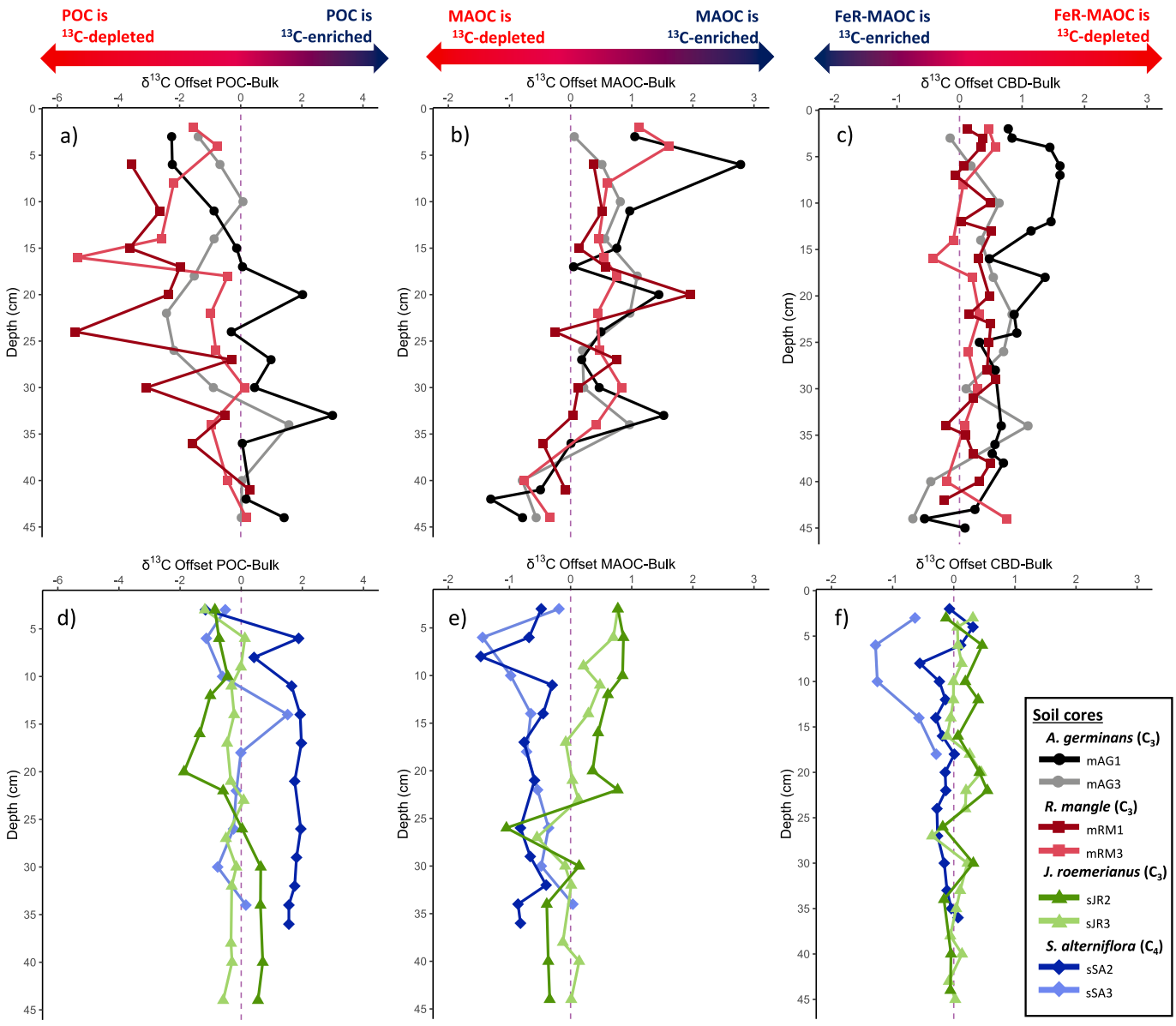

Fig. 7. Down-core variation in $\delta^{13}C_{offset}$ between POC, MAOC, FeR-MAOC, and bulk SOC in mangrove (a, b, c) and salt marsh soils (d, e, f).

root (t(14) = -2.70, p = 0.02; Fig. S4). However, this alone would not explain the downcore depletion of bulk SOC $\delta^{13}C$ below the depth of first *R. mangle* establishment (10.7 cm; Fig. S3). Apart from C_4 salt marshes, other possible sources of ^{13}C-enriched OC in coastal wetlands are algae and phytoplankton (Fry and Sherr, 1989; Matos et al., 2020). However, their contributions were likely minimal in our sampling sites, based on the predominance of long-chained *n*-alkanes (plant-derived) over short-chained *n*-alkanes (bacteria and algae-derived) (Assavapanuvat et al., unpublished results). The contribution of allochthonous terrestrial-derived OC to our soil samples is likely to be less important than autochthonous mangrove-salt marsh-derived OC because the $\delta^{13}C$ of Apalachicola riverine suspended particles was more $\delta^{13}C$-depleted (−28.0 ± 1.9 ‰ (Peterson et al., 2013) or −26.8 ± 2.4 ‰ (Arellano et al., 2019)) than our POC (–22.3 ± 4.4 ‰), MAOC (−21.8 ± 3.2 ‰), and bulk SOC (–22.0 ± 3.5 ‰) samples. Post-depositional partial decomposition of OC, in oxic and anoxic environments, can decrease bulk soil $\delta^{13}C$ due to preferential loss of ^{13}C-enriched labile organic molecules such as sugars and simple carbohydrates (Lehmann et al., 2002), while accumulation of microbial biomass (living and necromass) in aged soil could increase $\delta^{13}C$ (Bird et al., 2003; Ehleringer et al., 2000). However, both processes typically shift soil $\delta^{13}C$ by less than ~ 3 ‰ (Bird et al., 2003; Ehleringer et al., 2000; Kelleway et al., 2022; Lehmann et al., 2002), while our $\delta^{13}C$ increased with depth up to + 11.67 ‰ and + 9.40 ‰ in *A. germinans* and *R. mangle* habitats, respectively. This highlighted that post-depositional transformations were less important than the effects of plant replacement.

4.2. Plant-specific influences on stocks and origins of SOC sub-fractions

4.2.1. POC

Contrary to our hypothesis, POC was higher in unencroached salt marsh habitats relative to mangroves ($p < 0.0001$). Our findings contradict previous studies from the eastern Chinese coastline where larger POC fractions were observed in “mature native” mangrove soils compared to the soils of “young invasive” salt marshes (Feng et al., 2019; Fu et al., 2024). As our study site is experiencing an inverse vegetation replacement pattern compared to Chinese coastlines, higher POC content in our salt marsh soils may result from greater productivity of “mature native” salt marshes, relative to the “young encroaching” mangroves. An increasing soil POC content with the age of salt marsh

communities has also been reported in previous studies (Yang et al., 2017, 2016) (Table 2).

Apart from higher production of POC in salt marsh habitats, their elevated POC content may also result from slower degradation rate of salt marsh detritus relative to those of mangroves. Unlike the general expectation that mangrove materials are more intrinsically recalcitrant than salt marshes (Cui et al., 2021; Saraswati et al., 2016; Sun et al., 2019), several publications have reported faster decomposition rates in mangrove litter compared to salt marshes, attributed to lower lignin content in mangrove tissues (Ouyang et al., 2017; Perry and Mendelssohn, 2009; Simpson et al., 2021). Our findings support this trend with greater total lignin content (summation of vanillyl, syringyl, and cinnamyl lignin oxidation products: Λ_8) in *S. alterniflora* fresh tissues (Λ_8 = 9.7 ± 3.5 mg per 100 mg OC), compared to the tissues of *A. germinans*, *R. mangle*, and *J. roemerianus* (Λ_8 = 8.6 ± 1.9, 4.3 ± 3.1, 8.0 ± 2.5 mg per 100 mg OC respectively) (Assavapanuvat et al., unpublished results). Due to their perennial nature, salt marshes generally have higher belowground: aboveground productivity (Alongi, 2020) and higher root turnover rate relative to mangroves (Ouyang et al., 2017). This rapid root turnover results in accumulation of dead salt marsh roots in soils as POC, while mangrove roots tend to stay intact with the living trees. This agrees with past studies which proposed that SOC (Arnaud et al., 2023; Chen and Twilley, 1999; Simpson et al., 2020), as well as coastal wetland POC (Zhang et al., 2021), is principally derived from root-OC. Alternatively, higher accumulation of POC in salt marsh habitats may result from higher export of suspended OC and dissolved inorganic carbon (DIC) from mangrove habitats, relative to salt marshes, as observed in previous global (Alongi, 2020) and regional studies (Santos et al., 2021). Nevertheless, it should be noted that the calculation of POC fraction in our study was based on mass-balance between bulk SOC and MAOC. Hence, the POC fraction may be overestimated if some water-extractable OC was lost during the experiment (see Text S2 for further details on method artifacts). Estimations of POC-MAOC in much of the previous literature were based on different methods; some used different fractionation schemes while some others used different thresholds for particle sizes and density limits (Table 2). While the size-based POC-MAOC separation is more cost-efficient and better for examining the effect of thermodynamics (e.g., Ausín et al., 2021; Cotrufo et al., 2019), density-based method could provide deeper insight on OC interaction with various groups of soil minerals with different density (e.g., Sollins et al., 2006; Yeasmin et al., 2017). A standard protocol for POC and MAOC quantification is critically needed to help reconcile these differences in the literature and to better constrain estimates on global distribution of POC and MAOC in coastal wetland soils.

Across all plant habitats, greater C/N ratios in POC relative to bulk SOC suggested that POC was principally derived from the wetland plants. In C_3 mangrove soils, negative $\delta^{13}C_{offset}$ POC-bulk suggested that OC derived from recently established mangroves was selectively stored as POC, without association with mineral surfaces. The most negative $\delta^{13}C_{offset}$ POC-bulk was observed in *R. mangle* habitats (Fig. 7a), implying that *R. mangle* detritus was the least decomposable. *R. mangle* tissues have greater concentrations of phenolic compounds (e.g., tannins) than *A. germinans* and salt marshes (Friesen et al., 2018; Kristensen et al., 2008; Lacerda et al., 1995; McKee, 1996; Saraswati et al., 2016). The $\delta^{13}C_{offset}$ POC-bulk converged to zero or even became positive with depth in soil cores that experienced the replacement of C_3 plants by C_4 *S. alterniflora* (mAG1, mAG3, mRM1, mRM3, sJR2; Fig. 7a, 7d; Table S11). This indicated that POC in deep soil section was derived from the previous C_4 *S. alterniflora* communities.

4.2.2. MAOC

While plant species had no significant influence on whole-core MAOC content, the positive correlation between MAOC and the availability of fine soil particles (<53 μm) ($r = 0.62$, $p < 0.001$) highlighted the importance of inorganic mineral surface area as substrate for OC attachment and MAOC formation. The range of f_{MAOC} in our study is comparable with previous estimates in coastal wetland soils (Table 2). Unlike POC, MAOC appears to be derived from microbially-altered OC, likely derived from a mixture of microbial necromass (in vivo) and/or OC from the former plant community (ex vivo pathway). This speculation was supported by the observed shift in the $\delta^{13}C_{offset}$ MAOC-Bulk away from the present-day plant endmembers in most soil cores (Fig. 7b, 7e). In C_3 plant habitats, MAOC was principally made of ^{13}C-enriched OC, such as plant-derived simple sugars (e.g., Deines, 1980; Lehmann et al., 2002) and microbial biomass (Bird et al., 2003 and references therein; Dong et al., 2023). This finding aligns with the Microbial Efficiency Matrix Stabilization theory (Cotrufo et al., 2013), whereby MAOC is predominantly composed of labile OC. Accumulation of microbial OC in MAOC was also supported by lower C/N ratio of MAOC relative to bulk SOC and POC (Fig. 6), similar to the range of C/N ratios reported in the literature (Angst et al., 2021; Cotrufo et al., 2019; Lavallee et al., 2020; Mirabito and Chambers, 2023; Yang et al., 2016). The only exception was observed in soils from C_4 *S. alterniflora* habitats, where MAOC was more depleted in $\delta^{13}C$ than bulk OC. This might suggest that *S. alterniflora* MAOC was made of decomposed plant-derived OC (Angst et al., 2021), which was generally more $\delta^{13}C$-depleted than fresh plant litter (Lehmann et al., 2002). While Komada et al. (2022) observed that the majority of MAOC in minerogenic San Francisco salt marshes originated from allochthonous reworked OC, MAOC this study appears to be derived from local wetland C_4 vegetation because $\delta^{13}C_{MAOC}$ values were more enriched than allochthonous riverine particles from Apalachicola River, that drain the northern parts of the Apalachicola estuarine watershed (Arellano et al., 2019; Peterson et al., 2013). Nevertheless, further work on $\Delta^{14}C$-age of the MAOC fraction is still needed to better estimate the relative contribution of reworked old OC, from soil-derived watershed inputs, to the estuarine MAOC pool.

4.2.3. FeR-MAOC

The high abundance of FeR-MAOC in *A. germinans*, *S. alterniflora*, and *J. roemerianus* soils may reflect the promotion of FeR-MAOC formation by oxygen release from plant's rhizosphere. In coastal wetland soils, FeR-MAOC formation could be intensified at redox interfaces where dissolved OC (DOC) interacts with dissolved iron (Fe(II)) and oxygen, then subsequently precipitates Fe(III) with OC (Barber et al., 2017; Li et al., 2023; Riedel et al., 2013). In vegetated coastal habitats, sources of oxygen that promotes this mechanism may derive from radial oxygen loss from plant roots (Spivak et al., 2019). The existence of oxygen release from the plant's rhizosphere, in the subsurface reducing zone, was confirmed by the co-occurrence of reduced (pyrite) and oxidized (FeR and Fe (III)) minerals (Fig. 2). Previous studies have showed higher oxygen release (i.e., higher soil Eh) in *A. germinans* habitats compared to the salt marshes (Table S12); however, this pattern has not been universally confirmed, as it depends on site-specific conditions and plant maturity (Alongi et al., 2000; Comeaux et al., 2012; Friesen et al., 2018; Koretsky et al., 2008; Krauss et al., 2006; Lacerda et al., 1993; Perry and Mendelssohn, 2009; Rietl et al., 2016; Thibodeau and Nickerson, 1986). Larger fractions of FeR-MAOC in *S. alterniflora* soils have been observed compared to the other salt marshes (Chen et al., 2024), while another study reported larger fractions of FeR-MAOC in *Kandelia obovata* mangrove soils relative to *S. alterniflora* habitats (Lin et al., 2023) (Table 3). In our study, no difference in FeR-MAOC content was observed among *A. germinans*, *S. alterniflora*, and *J. roemerianus* habitats. This suggests that the promotion of FeR-MAOC formation by an oxidizing rhizosphere does not have a clear universal plant-species-dependent pattern. The fraction of FeR-MAOC (~10 % of OC_{Bulk}) in our shallow soil samples was slightly lower, yet still comparable with previous estimates of FeR-MAOC in mangroves, salt marshes, and plant rhizospheric soils (Table 3).

The paucity of FeR-MAOC in *R. mangle* habitats (Fig. 5) may reflect minimal releases of oxygen from *R. mangle* roots. Previous work has also shown more reducing conditions in *R. mangle* soils compared to

A. germinans and salt marsh soils (Table S12) (Alongi et al., 2000; Comeaux et al., 2012; Friesen et al., 2018; Krauss et al., 2006; Lacerda et al., 1993; Perry and Mendelssohn, 2009; Thibodeau and Nickerson, 1986). This conflicts with our findings that showed the highest concentrations of CBD-extractable reactive iron in *R. mangle* soils (Fig. 2), suggesting that redox potential was not the only factor that regulated FeR-MAOC stocks. Alternatively, we speculate that *R. mangle* soils had the lowest FeR-MAOC formation efficiency due to the interference at iron-OC interaction sites by phenolic compounds (e.g., tannins). It is well known that *R. mangle* leaves and litter have greater amounts of tannins compared to *A. germinans* and other salt marshes (Friesen et al., 2018; Kristensen et al., 2008; Lacerda et al., 1995; McKee, 1996). During litter decomposition and leaching, these phenolic compounds may coagulate with freshly precipitated reactive iron at the sediment redox interface (Riedel et al., 2013). Hydrophilic phenolic compounds can rapidly saturate the sorption sites of FeR mineral surfaces, while the sorption of hydrophobic compounds (e.g., long-chained fatty acids from plant wax) can allow for the buildup of multilayered hemimicelles (Day et al., 1994; Evanko and Dzombak, 1998). Hence, the pre-occupancy of sorption sites by phenolic leachates is expected to hinder the sorption of new OC on FeR surface, thereby minimizing the FeR-MAOC fraction in *R. mangle* soils. The sorption of phenolic compounds on FeR surface would also stabilize reactive iron minerals against reductive dissolution, allowing reactive iron to accumulate in *R. mangle* soils – despite the evidence of reducing conditions – as suggested by Mössbauer spectra (Fig. 2). Despite the lack of direct evidence here, we confirmed the accumulation of tannins in *R. mangle* soil by high concentration of 3,5-dihydroxybenzoic acid (3,5-Bd), a biomarker of tannins (Goñi and Hedges, 1995; Houel et al., 2006; Louchouarn et al., 1999). Further work is needed to show the prevalence of phenolic moities on FeR surface (e.g., using Fourier transform infrared spectroscopy [FTIR]), to better substantiate the role of tannins. Alternatively, low FeR-MAOC content in *R. mangle* habitats may have resulted from the release of root exudates, such as oxalic acids and catechols, which are efficient in MAOC and FeR-MAOC destabilization, (Chari and Taylor, 2022; Keiluweit et al., 2015; Li et al., 2021; Yuan et al., 2022). This remains speculative, as we have no information on the chemical composition of *R. mangle* root exudates.

Although MAOC was dominated by decomposed SOC and microbial biomass (section 4.2.2), the majority of FeR-MAOC may have been formed through the co-precipitation of reactive iron with fresh soluble OC released to soils, from living plants, in an oxidizing rhizosphere. This fresh soluble OC might include rhizodeposits, which have been reported to have higher MAOC formation efficiency compared to leaf and root biomass (Villarino et al., 2021). The significant positive and negative $\delta^{13}C_{offset}$ CBD-Bulk in the shallow soil section of core mAG1 and sSA3, respectively, suggest preferential retention of C_3 *A. germinans* and C_4 *S. alterniflora*-derived OC with reactive iron (Fig. 7c, 7f, Table S11). This implies that plant-mediated FeR-MAOC formation preferentially incorporated plant-derived OC into FeR-MAOC, but did not facilitate the stabilization of pre-aged OC that existed prior to the development of plant rhizosphere. This finding agrees with other work that showed higher FeR-MAOC content in the rhizosphere of freshwater wetland plants compared to the soils outside root influences (Duan et al., 2020).

4.3. MAOC formation with reactive iron phases versus other minerals

While the plant rhizosphere can promote the formation of FeR-MAOC, this mechanism did not stabilize the entire stock of SOC in all plant habitats. FeR-MAOC was only a small fraction of MAOC, representing 13.74 ± 15.55 % % of total MAOC. These estimates were significantly lower than FeR-$MAOC_{max}$ which was 29.77 ± 27.41 % of total MAOC ($t(96) = 7.29$, $p < 0.001$). These differences may reflect dramatic loss of mineral-bound OC during the NaCl control treatment (Fisher et al., 2020). This loss may suggest that a considerable amount of OC was "weakly" bound to reactive iron or other soil minerals, and were solubilized during the NaCl treatment (Fisher et al., 2020). Both FeR-MAOC and FeR-$MAOC_{max}$ were less than half of total MAOC, highlighting that the majority of MAOC (~86.71 ± 15.07 %) in both mangrove and salt marsh habitats is in association with other soil minerals that are not reactive iron (oxy)hydroxides (nonFeR-MAOC). This nonFeR-MAOC could be clay-bound MAOC (clay-MAOC). Nevertheless, a recent study, which performed sequential extraction of FeR-MAOC (through CBD method) and clay-MAOC (through HF-solubilization method), indicated that the clay-MAOC fraction was smaller than FeR-MAOC (FeR-MAOC and clay-MAOC were 18.8 ± 1.1 % and 11.9 ± 1.2 % of total SOC, respectively) (Zhu et al., 2023). Despite the lack of direct evidence, this may indicate that the majority of MAOC is associated with other classes of soil minerals that are neither reactive iron nor clay. This "hidden MAOC" may include calcium-MAOC (Wang et al., 2021), iron-sulfide-MAOC (Picard et al., 2019), and/or sulfurized SOC (Raven et al., 2019) that were previously observed in wetland soils, yet these fractions remain largely unexplored. Further research on these "hidden" forms of non-FeR-MAOC is needed, as this OC pool may be important for long-term storage blue carbon storage due in part, to their high stability under redox fluctuations and future sea level rise. The existence of this hidden non-FeR-MAOC must be confirmed with artifact evaluation of FeR-MAOC and clay-MAOC extraction methods.

4.4. SOC vulnerability and stabilization mechanisms following mangrove-salt marsh replacement

The initial stages of mangrove-salt marsh transition, along the southeastern coast of the USA, began with the establishment of *A. germinans* (Bardou et al., 2021). In this early stage of *A. germinans* succession (~34 years after the first *A. germinans* record), SOC stocks, sub-fractions, and stabilization mechanisms were not substantially altered (Fig. 8). However, future carbon dynamics may be seriously altered with the maturation of the *A. germinans* community. As climate warming progressed, *R. mangle* establishment was documented several years after the first occurrence of *A. germinans* on the southeastern n coast of the U.S. (Bardou et al., 2021; Osland et al., 2018; Snyder et al., 2021). The colonization of *R. mangle* may immediately change SOC composition and stabilization mechanisms (within ~ 12 years from the first *R. mangle* record). High sediment trapping efficiency by *R. mangle* root system may increase OC burial rate. The establishment of *R. mangle* may also decrease FeR-MAOC stock; thus, OC in *R. mangle* habitats is not susceptible to reductive destabilization in sea level rise scenario. On the other hand, sea level rise may promote POC accumulation in *R. mangle* habitats due to the "Enzymatic latch hypothesis" (Dasat and Sam, 2022; Saraswati et al., 2016). Compared with *A. germinans* habitats, recent work observed that the accumulation of phenolic leachates in *R. mangle* habitats resulted in stronger inhibition of microbial hydrolytic enzymes and enhanced overall OC preservation (Dasat and Sam, 2022). Nevertheless, further research is needed to validate our hypothesis.

5. Conclusion

In the past few decades, the Apalachicola barrier islands have experienced the replacement of *S. alterniflora* salt marshes by *A. germinans* and *R. mangle* mangroves due to less frequent freezing events. This region also experienced reciprocal substitution of *S. alterniflora* by *J. roemerianus* salt marshes, possibly driven by sea level rise and/or elevation change. Mangrove encroachment may increase OC burial by promoting the formation of SOC by vertical particle trapping. In contrast, unencroached mature salt marshes contributed more OC to soils via belowground processes, resulting in higher OC stocks with greater POC fractions. OC derived from recently established plant communities was preferentially stored as POC. However, microbially-transformed OC, partially from previous plant habitats, was dominated in the MAOC fraction. Oxygen release from the *A. germinans*, *S. alterniflora*, and *J. roemerianus* rhizospheres preferentially promoted

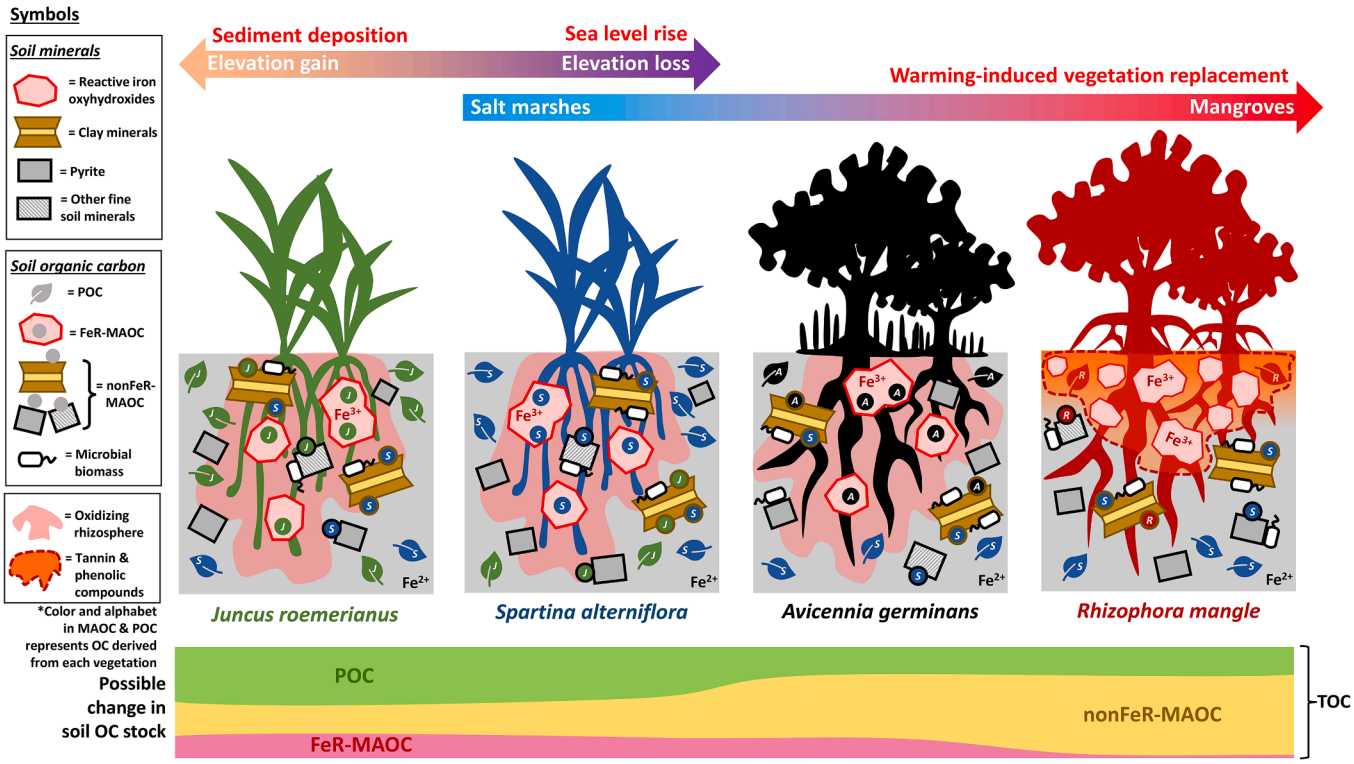

Fig. 8. Conceptual model illustrates evolution of SOC composition, and changes in relative importance of each SOC sub-fraction under the influences of warming-induced vegetation replacement and sea level rise. The top arrows represent trends of plant succession according to downcore $\delta^{13}C$ variation. The middle illustrations describe the content and .
Sources of POC, MAOC, and FeR-MAOC, differentiated by representative color and alphabet of each plant. The total thickness of the color bar at the bottom represents total SOC stock, while each color represents proportion of each SOC sub-fractions in total SOC

the precipitation of their freshly released dissolved OC with FeR; with little evidence of FeR-MAOC from previous plant communities. Considering all this evidence, our study offers new insights on the roles of different OC origins in organo-mineral stabilization mechanisms of SOC, with emphasis on taxon-specific effects of different mangroves and salt marshes species.

CRediT authorship contribution statement

Prakhin Assavapanuvat: Writing – original draft, Visualization, Methodology, Formal analysis, Conceptualization. **Joshua L. Breithaupt:** Writing – review & editing, Methodology, Conceptualization. **Kevin M. Engelbert:** Writing – review & editing, Methodology. **Christian Schröder:** Writing – review & editing, Methodology. **Joseph M. Smoak:** Writing – review & editing, Methodology. **Thomas S. Bianchi:** Writing – review & editing, Supervision, Funding acquisition, Conceptualization.

Declaration of competing interest

The authors declare that they have no known competing financial interests or personal relationships that could have appeared to influence the work reported in this paper.

Acknowledgement

This work was funded by the Jon and Beverly L. Thompson Endowed Chair of Geological Sciences. JLB and KME were supported by the Triumph Gulf Coast Inc., Project #69: Apalachicola Bay System Initiative. C.S. acknowledges funding by the UK Space Agency (ST/Y000072/1). Instrumentation and interpretation of raw stable isotope and ICP-MS data were supported by Jason Curtis and George Kamenov, Department of Geological Sciences, University of Florida, respectively. Field data acquisition was assisted by Havalend E. Steinmuller and the members of Coastal and Marine Laboratory, Florida State University. Thanks to David R. Atherton, João H. L. Amaral, Emily G. Watts, Jacob R. Gaddy, and the other current and past members of Bianchi's lab group for the discussion on laboratory methods and data interpretations. This article greatly benefited from the comments and suggestions of 3 anonymous reviewers and the editor, Dr. Cornelia Rumpel, for which we are grateful.

Appendix A. Supplementary data

Supplementary data to this article can be found online at https://doi.org/10.1016/j.geoderma.2024.116904.

References

Alongi, D.M., 2020. Carbon Balance in Salt Marsh and Mangrove Ecosystems: A Global Synthesis. JMSE 8, 767. https://doi.org/10.3390/jmse8100767.
Alongi, D.M., Tirendi, F., Clough, B.F., 2000. Below-ground decomposition of organic matter in forests of the mangroves Rhizophora stylosa and Avicennia marina along the arid coast of Western Australia. Aquat. Bot. 68, 97–122. https://doi.org/10.1016/S0304-3770(00)00110-8.
Angst, G., Mueller, K.E., Nierop, K.G.J., Simpson, M.J., 2021. Plant- or microbial-derived? A review on the molecular composition of stabilized soil organic matter. Soil Biol. Biochem. 156, 108189 https://doi.org/10.1016/j.soilbio.2021.108189.
Appleby, P., Oldfield, F., 1992. Applications of lead-210 to sedimentation studies, in: Uranium-Series Disequilibrium: Applications to Earth, Marine, and Environmental Sciences. 2. Ed.
Appleby, P., Nolan, P., Oldfield, F., Richardson, N., Higgitt, S., 1988. 210Pb dating of lake sediments and ombrotrophic peats by gamma essay. Sci. Total Environ. 69, 157–177. https://doi.org/10.1016/0048-9697(88)90341-5.
Arellano, A.R., Bianchi, T.S., Osburn, C.L., D'Sa, E.J., Ward, N.D., Oviedo-Vargas, D., Joshi, I.D., Ko, D.S., Shields, M.R., Kurian, G., Green, J., 2019. Mechanisms of Organic Matter Export in Estuaries with Contrasting Carbon Sources. JGR Biogeosciences 124, 3168–3188. https://doi.org/10.1029/2018JG004868.

Arnaud, M., Krause, S., Norby, R.J., Dang, T.H., Acil, N., Kettridge, N., Gauci, V., Ullah, S., 2023. Global mangrove root production, its controls and roles in the blue carbon budget of mangroves. Glob. Chang. Biol. 29, 3256–3270. https://doi.org/10.1111/gcb.16701.

Ausín, B., Bruni, E., Haghipour, N., Welte, C., Bernasconi, S.M., Eglinton, T.I., 2021. Controls on the abundance, provenance and age of organic carbon buried in continental margin sediments. Earth Planet. Sci. Lett. 558, 116759 https://doi.org/10.1016/j.epsl.2021.116759.

Bai, J., Luo, M., Yang, Y., Xiao, S., Zhai, Z., Huang, J., 2021. Iron-bound carbon increases along a freshwater–oligohaline gradient in a subtropical tidal wetland. Soil Biol. Biochem. 154, 108128 https://doi.org/10.1016/j.soilbio.2020.108128.

Barber, A., Brandes, J., Leri, A., Lalonde, K., Balind, K., Wirick, S., Wang, J., Gélinas, Y., 2017. Preservation of organic matter in marine sediments by inner-sphere interactions with reactive iron. Sci. Rep. 7, 366. https://doi.org/10.1038/s41598-017-00494-0.

Bardou, R., Parker, J.D., Feller, I.C., Cavanaugh, K.C., 2021. Variability in the fundamental versus realized niches of North American mangroves. J. Biogeogr. 48, 160–175. https://doi.org/10.1111/jbi.13990.

Bianchi, T.S., Allison, M.A., Zhao, J., Li, X., Comeaux, R.S., Feagin, R.A., Kulawardhana, R.W., 2013. Historical reconstruction of mangrove expansion in the Gulf of Mexico: Linking climate change with carbon sequestration in coastal wetlands. Estuar. Coast. Shelf Sci. 119, 7–16. https://doi.org/10.1016/j.ecss.2012.12.007.

Bird, M., Kracht, O., Derrien, D., Zhou, Y., 2003. The effect of soil texture and roots on the stable carbon isotope composition of soil organic carbon. Aust. J. Soil Res. 41, 77. https://doi.org/10.1071/SR02044.

Breithaupt, J.L., Smoak, J.M., Smith, T.J., Sanders, C.J., 2014. Temporal variability of carbon and nutrient burial, sediment accretion, and mass accumulation over the past century in a carbonate platform mangrove forest of the Florida Everglades: Carbon Burial in the Coastal Everglades. JGR Biogeosciences. 119, 2032–2048. https://doi.org/10.1002/2014JG002715.

Breithaupt, J.L., Smoak, J.M., Bianchi, T.S., Vaughn, D.R., Sanders, C.J., Radabaugh, K. R., Osland, M.J., Feher, L.C., Lynch, J.C., Cahoon, D.R., Anderson, G.H., Whelan, K. R.T., Rosenheim, B.E., Moyer, R.P., Chambers, L.G., 2020. Increasing Rates of Carbon Burial in Southwest Florida Coastal Wetlands. JGR Biogeosciences. 125 https://doi.org/10.1029/2019JG005349.

Breithaupt, J.L., Steinmuller, H.E., 2022. Refining the Global Estimate of Mangrove Carbon Burial Rates Using Sedimentary and Geomorphic Settings. Geophys. Res. Lett. 49 https://doi.org/10.1029/2022GL100177.

Cambardella, C.A., Elliott, E., 1992. Particulate soil organic-matter changes across a grassland cultivation sequence. Soil Sci. Soc. Am. J. 56, 777–783. https://doi.org/10.2136/sssaj1992.03615995005600030017x.

Canfield, D.E., 1989. Reactive iron in marine sediments. Geochim. Cosmochim. Acta 53, 619–632. https://doi.org/10.1016/0016-7037(89)90005-7.

Canty, A., Ripley, B.D., 2022. boot: Bootstrap R (S-Plus) Functions.

Cavanaugh, K.C., Kellner, J.R., Forde, A.J., Gruner, D.S., Parker, J.D., Rodriguez, W., Feller, I.C., 2014. Poleward expansion of mangroves is a threshold response to decreased frequency of extreme cold events. PNAS 111, 723–727. https://doi.org/10.1073/pnas.1315800111.

Chari, N.R., Taylor, B.N., 2022. Soil organic matter formation and loss are mediated by root exudates in a temperate forest. Nat. Geosci. 15, 1011–1016. https://doi.org/10.1038/s41561-022-01079-x.

Chen, X., Alizad, K., Wang, D., Hagen, S.C., 2014. Climate Change Impact on Runoff and Sediment Loads to the Apalachicola River at Seasonal and Event Scales. J. Coast. Res. 68, 35–42. https://doi.org/10.2112/SI68-005.1.

Chen, C., Hall, S.J., Coward, E., Thompson, A., 2020. Iron-mediated organic matter decomposition in humid soils can counteract protection. Nat. Commun. 11, 2255. https://doi.org/10.1038/s41467-020-16071-5.

Chen, R., Twilley, R.R., 1999. A simulation model of organic matter and nutrient accumulation in mangrove wetland soils. Biogeochemistry 44, 93–118. https://doi.org/10.1007/BF00993000.

Chen, G., Zhang, M., Yao, X., Zhu, Y., Hu, Y., Hui, D., Li, J., Chen, J., Deng, Q., 2023. Soil Organic Carbon Sequestration after 20-Year Afforestation of Mangrove Plantations on Qi'ao Island. Southern China. Agronomy 13, 2389. https://doi.org/10.3390/agronomy13092389.

Chen, W., Zhang, W., Qiu, Y., Shu, Z., Liu, J., Zhang, X., Waqas, K., Song, G., 2024. How does exotic Spartina alterniflora affect the contribution of iron-bound organic carbon to soil organic carbon in salt marshes? Sci. Total Environ. 926, 171605 https://doi.org/10.1016/j.scitotenv.2024.171605.

Comeaux, R.S., Allison, M.A., Bianchi, T.S., 2012. Mangrove expansion in the Gulf of Mexico with climate change: Implications for wetland health and resistance to rising sea levels. Estuar. Coast. Shelf Sci. 96, 81–95. https://doi.org/10.1016/j.ecss.2011.10.003.

Cotrufo, M.F., Wallenstein, M.D., Boot, C.M., Denef, K., Paul, E., 2013. The Microbial Efficiency-Matrix Stabilization (MEMS) framework integrates plant litter decomposition with soil organic matter stabilization: do labile plant inputs form stable soil organic matter? Glob. Chang. Biol. 19, 988–995. https://doi.org/10.1111/gcb.12113.

Cotrufo, M.F., Soong, J.L., Horton, A.J., Campbell, E.E., Haddix, M.L., Wall, D.H., Parton, W.J., 2015. Formation of soil organic matter via biochemical and physical pathways of litter mass loss. Nat. Geosci. 8, 776–779. https://doi.org/10.1038/ngeo2520.

Cotrufo, M.F., Ranalli, M.G., Haddix, M.L., Six, J., Lugato, E., 2019. Soil carbon storage informed by particulate and mineral-associated organic matter. Nat. Geosci. 12, 989–994. https://doi.org/10.1038/s41561-019-0484-6.

Cui, L., Sun, H., Du, X., Feng, W., Wang, Y., Zhang, J., Jiang, J., 2021. Dynamics of labile soil organic carbon during the development of mangrove and salt marsh ecosystems. Ecol. Ind. 129, 107875 https://doi.org/10.1016/j.ecolind.2021.107875.

Dasat, G.S., Sam, C.E., 2022. Carbon sequestration and the enzymic latch mechanism in red, black and white mangrove soils of Florida USA. World Journal of Advanced Research and Reviews 13, 421–430. https://doi.org/10.30574/wjarr.2022.13.3.0235.

Day, G.M., Hart, B.T., McKelvie, I.D., Beckett, R., 1994. Adsorption of natural organic matter onto goethite. Colloids Surf A Physicochem Eng Asp 89, 1–13. https://doi.org/10.1016/0927-7757(94)02855-9.

de Lacerda, L., Carvalho, C., Tanizaki, K., Ovalle, A., Rezende, C., 1993. The biogeochemistry and trace metals distribution of mangrove rhizospheres. Biotropica 252–257. https://doi.org/10.2307/2388783.

Deines, P., 1980. The isotopic composition of reduced organic carbon. Handbook of Environmental Isotope geochemistry.

Dicen, G.P., Navarrete, I.A., Rallos, R.V., Salmo, S.G., Garcia, M.C.A., 2019. The role of reactive iron in long-term carbon sequestration in mangrove sediments. J. Soil. Sediment. 19, 501–510. https://doi.org/10.1007/s11368-018-2051-y.

Dong, H., Zeng, Q., Sheng, Y., Chen, C., Yu, G., Kappler, A., 2023. Coupled iron cycling and organic matter transformation across redox interfaces. Nature Reviews Earth & Environment 4, 659–673. https://doi.org/10.1038/s43017-023-00470-5.

Dontis, E.E., Radabaugh, K.R., Chappel, A.R., Russo, C.E., Moyer, R.P., 2020. Carbon Storage Increases with Site Age as Created Salt Marshes Transition to Mangrove Forests in Tampa Bay, Florida (USA). Estuar. Coasts 43, 1470–1488. https://doi.org/10.1007/s12237-020-00733-0.

Doughty, C.L., Langley, J.A., Walker, W.S., Feller, I.C., Schaub, R., Chapman, S.K., 2016. Mangrove Range Expansion Rapidly Increases Coastal Wetland Carbon Storage. Estuar. Coasts 39, 385–396. https://doi.org/10.1007/s12237-015-9993-8.

Drexler, J.Z., Fuller, C.C., Archfield, S., 2018. The approaching obsolescence of 137Cs dating of wetland soils in North America. Quat. Sci. Rev. 199, 83–96. https://doi.org/10.1016/j.quascirev.2018.08.028.

Duan, X., Yu, X., Li, Z., Wang, Q., Liu, Z., Zou, Y., 2020. Iron-bound organic carbon is conserved in the rhizosphere soil of freshwater wetlands. Soil Biol. Biochem. 149, 107949 https://doi.org/10.1016/j.soilbio.2020.107949.

Duarte, C.M., Middelburg, J.J., Caraco, N., 2005. Major role of marine vegetation on the oceanic carbon cycle. Biogeosciences 2, 1–8. https://doi.org/10.5194/bg-2-1-2005.

Duarte, C.M., Losada, I.J., Hendriks, I.E., Mazarrasa, I., Marbà, N., 2013. The role of coastal plant communities for climate change mitigation and adaptation. Nat. Clim. Chang. 3, 961–968. https://doi.org/10.1038/nclimate1970.

Edmiston, H.L., Fahrny, S.A., Lamb, M.S., Levi, L.K., Wanat, J.M., Avant, J.S., Wren, K., Selly, N.C., 2008. Tropical Storm and Hurricane Impacts on a Gulf Coast Estuary: Apalachicola Bay, Florida. J. Coast. Res. 10055, 38–49. https://doi.org/10.2112/SI55-009.1.

Ehleringer, J.R., Buchmann, N., Flanagan, L.B., 2000. Carbon isotope ratios in belowground carbon cycle processes. Ecol. Appl. 10, 412–422. https://doi.org/10.1890/1051-0761(2000)010[0412:CIRIBC]2.0.CO;2.

Evanko, C.R., Dzombak, D.A., 1998. Influence of structural features on sorption of NOM-analogue organic acids to goethite. Environ. Sci. Tech. 32, 2846–2855. https://doi.org/10.1021/es980256t.

Feng, J., Wang, S., Wang, S., Ying, R., Yin, F., Jiang, L., Li, Z., 2019. Effects of Invasive *Spartina alterniflora* Loisel. and Subsequent Ecological Replacement by *Sonneratia apetala* Buch.-Ham. on Soil Organic Carbon Fractions and Stock. Forests 10, 171. https://doi.org/10.3390/f10020171.

Fisher, B.J., Moore, O.W., Faust, J.C., Peacock, C.L., März, C., 2020. Experimental evaluation of the extractability of iron bound organic carbon in sediments as a function of carboxyl content. Chem. Geol. 556, 119853 https://doi.org/10.1016/j.chemgeo.2020.119853.

Friesen, S.D., Dunn, C., Freeman, C., 2018. Decomposition as a regulator of carbon accretion in mangroves: a review. Ecol. Eng. 114, 173–178. https://doi.org/10.1016/j.ecoleng.2017.06.069.

Fry, B., Sherr, E.B., 1989. δ13C measurements as indicators of carbon flow in marine and freshwater ecosystems. Stable Isotopes in Ecological Research. Springer 196–229.

Fu, C., Li, Y., Zeng, L., Tu, C., Wang, X., Ma, H., Xiao, L., Christie, P., Luo, Y., 2024. Climate and mineral accretion as drivers of mineral-associated and particulate organic matter accumulation in tidal wetland soils. Glob. Chang. Biol. 30, e17070.

Furukawa, K., Wolanski, E., 1996. Sedimentation in mangrove forests. Mangrove Salt Marshes 1, 3–10. https://doi.org/10.1023/A:1025973426404.

Geldenhuys, C., Cotiyane, P., Rajkaran, A., 2016. Understanding the creek dynamics and environmental characteristics that determine the distribution of mangrove and salt marsh communities at Nahoon Estuary. S. Afr. J. Bot. 107, 137–147. https://doi.org/10.1016/j.sajb.2016.04.013.

Goñi, M.A., Hedges, J.I., 1995. Sources and reactivities of marine-derived organic matter in coastal sediments as determined by alkaline CuO oxidation. Geochim. Cosmochim. Acta 59, 2965–2981. https://doi.org/10.1016/0016-7037(95)00188-3.

Gütlich, P., Schröder, C., 2012. Mössbauer Spectroscopy, in: Schäfer, R., Schmidt, P.C. (Eds.), Methods in Physical Chemistry. Wiley, pp. 351–389. https://doi.org/10.1002/9783527636839.ch11.

Gütlich, P., Schröder, C., Schünemann, V., 2012. Mössbauer spectroscopy—an indispensable tool in solid state research. Spectrosc. Eur. 24, 21.

Harris, D., Horwáth, W.R., Van Kessel, C., 2001. Acid fumigation of soils to remove carbonates prior to total organic carbon or carbon-13 isotopic analysis. Soil Sci. Soc. Am. J. 65, 1853–1856. https://doi.org/10.2136/sssaj2001.1853.

Houel, S., Louchouarn, P., Lucotte, M., Canuel, R., Ghaleb, B., 2006. Translocation of soil organic matter following reservoir impoundment in boreal systems: Implications for in situ productivity. Limnol. Oceanogr. 51, 1497–1513. https://doi.org/10.4319/lo.2006.51.3.1497.

Hovenga, P.A., Wang, D., Medeiros, S.C., Hagen, S.C., Alizad, K., 2016. The response of runoff and sediment loading in the Apalachicola River, Florida to climate and land use land cover change: RESPONSES TO CLIMATE AND LULC CHANGE. Earth's Future 4, 124–142. https://doi.org/10.1002/2015EF000348.

Hu, D., Lan, W., Luo, M., Fan, T., Chen, X., Tan, J., Li, S., Guo, P., Huang, J., 2023. Increase in iron-bound organic carbon content under simulated sea-level rise: A "marsh organ" field experiment. Soil Biol. Biochem. 187, 109217 https://doi.org/10.1016/j.soilbio.2023.109217.

Huang, X., Liu, X., Liu, J., Chen, H., 2021. Iron-bound organic carbon and their determinants in peatlands of China. Geoderma 391, 114974. https://doi.org/10.1016/j.geoderma.2021.114974.

James, F., 2004. MINUIT Tutorial, Function Minimization, in: CERN Computing and Data Processing School. Pertisau, pp. 10–24.

Jimenez, L.C.Z., Queiroz, H.M., Otero, X.L., Nóbrega, G.N., Ferreira, T.O., 2021. Soil organic matter responses to mangrove restoration: A replanting experience in Northeast Brazil. Int. J. Environ. Res. Public Health 18, 8981. https://doi.org/10.3390/ijerph18178981.

Keiluweit, M., Bougoure, J.J., Nico, P.S., Pett-Ridge, J., Weber, P.K., Kleber, M., 2015. Mineral protection of soil carbon counteracted by root exudates. Nat. Clim. Chang. 5, 588–595. https://doi.org/10.1038/nclimate2580.

Kelleway, J.J., Saintilan, N., Macreadie, P.I., Skilbeck, C.G., Zawadzki, A., Ralph, P.J., 2016. Seventy years of continuous encroachment substantially increases 'blue carbon' capacity as mangroves replace intertidal salt marshes. Glob. Chang. Biol. 22, 1097–1109. https://doi.org/10.1111/gcb.13158.

Kelleway, J.J., Trevathan-Tackett, S.M., Baldock, J., Critchley, L.P., 2022. Plant litter composition and stable isotope signatures vary during decomposition in blue carbon ecosystems. Biogeochemistry 158, 147–165. https://doi.org/10.1007/s10533-022-00890-3.

Kida, M., Fujitake, N., 2020. Organic Carbon Stabilization Mechanisms in Mangrove Soils: A Review. Forests 11, 981. https://doi.org/10.3390/f11090981.

Kleber, M., Bourg, I.C., Coward, E.K., Hansel, C.M., Myneni, S.C.B., Nunan, N., 2021. Dynamic interactions at the mineral–organic matter interface. Nature Reviews Earth & Environment 2, 402–421. https://doi.org/10.1038/s43017-021-00162-y.

Klingelhöfer, G., Morris, R.V., Bernhardt, B., Rodionov, D., de Souza Jr, P.A., Squyres, S. W., Foh, J., Kankeleit, E., Bonnes, U., Gellert, R., 2003. Athena MIMOS II Mössbauer spectrometer investigation. JGR Planets 108. https://doi.org/10.1029/2003JE002138.

Komada, T., Bravo, A., Brinkmann, M., Lu, K., Wong, L., Shields, G., 2022. "Slow" and "fast" in blue carbon: Differential turnover of allochthonous and autochthonous organic matter in minerogenic salt marsh sediments. Limnol. Oceanogr. 67, S133–S147. https://doi.org/10.1002/lno.12090.

Koretsky, C.M., Haveman, M., Cuellar, A., Beuving, L., Shattuck, T., Wagner, M., 2008. Influence of Spartina and Juncus on Saltmarsh Sediments. I. Pore Water Geochemistry. Chemical Geology 255, 87–99. https://doi.org/10.1016/j.chemgeo.2008.06.013.

Krauss, K.W., Allen, J.A., Cahoon, D.R., 2003. Differential rates of vertical accretion and elevation change among aerial root types in Micronesian mangrove forests. Estuar. Coast. Shelf Sci. 56, 251–259. https://doi.org/10.1016/S0272-7714(02)00184-1.

Krauss, K.W., Doyle, T.W., Twilley, R.R., Rivera-Monroy, V.H., Sullivan, J.K., 2006. Evaluating the relative contributions of hydroperiod and soil fertility on growth of south Florida mangroves. Hydrobiologia 569, 311–324. https://doi.org/10.1007/s10750-006-0139-7.

Kristensen, E., Bouillon, S., Dittmar, T., Marchand, C., 2008. Organic carbon dynamics in mangrove ecosystems: A review. Aquat. Bot. 89, 201–219. https://doi.org/10.1016/j.aquabot.2007.12.005.

Lacerda, L., Ittekkot, V., Patchineelam, S., 1995. Biogeochemistry of Mangrove Soil Organic Matter: a Comparison BetweenRhizophoraandAvicenniaSoils in South-eastern Brazil. Estuar. Coast. Shelf Sci. 40, 713–720. https://doi.org/10.1006/ecss.1995.0048.

Lalonde, K., Mucci, A., Ouellet, A., Gélinas, Y., 2012. Preservation of organic matter in sediments promoted by iron. Nature 483, 198–200. https://doi.org/10.1038/nature10855.

Lavallee, J.M., Conant, R.T., Paul, E.A., Cotrufo, M.F., 2018. Incorporation of shoot versus root-derived 13C and 15N into mineral-associated organic matter fractions: results of a soil slurry incubation with dual-labelled plant material. Biogeochemistry 137, 379–393. https://doi.org/10.1007/s10533-018-0428-z.

Lavallee, J.M., Soong, J.L., Cotrufo, M.F., 2020. Conceptualizing soil organic matter into particulate and mineral-associated forms to address global change in the 21st century. Glob. Chang. Biol. 26, 261–273. https://doi.org/10.1111/gcb.14859.

Lehmann, M.F., Bernasconi, S.M., Barbieri, A., McKenzie, J.A., 2002. Preservation of organic matter and alteration of its carbon and nitrogen isotope composition during simulated and in situ early sedimentary diagenesis. Geochim. Cosmochim. Acta 66, 3573–3584.

Li, H., Bölscher, T., Winnick, M., Tfaily, M.M., Cardon, Z.G., Keiluweit, M., 2021. Simple Plant and Microbial Exudates Destabilize Mineral-Associated Organic Matter via Multiple Pathways. Environ. Sci. Tech. 55, 3389–3398. https://doi.org/10.1021/acs.est.0c04592.

Li, Q., Hu, W., Li, L., Li, Y., 2023. Interactions between organic matter and Fe oxides at soil micro-interfaces: Quantification, associations, and influencing factors. Sci. Total Environ. 855, 158710 https://doi.org/10.1016/j.scitotenv.2022.158710.

Lin, M., Chen, Y., Cheng, L., Zheng, Y., Wang, W., Sardans, J., Song, Z., Guggenberger, G., Zou, Y., Ding, X., Tariq, A., Zeng, F., Fahad Alrefaei, A., Peñuelas, J., 2023. Response of topsoil Fe-bound organic carbon pool and microbial community to Spartina alterniflora invasion in coastal wetlands. Catena 232, 107414. https://doi.org/10.1016/j.catena.2023.107414.

Louchouarn, P., Lucotte, M., Farella, N., 1999. Historical and geographical variations of sources and transport of terrigenous organic matter within a large-scale coastal environment. Org Geochem. 30, 675–699. https://doi.org/10.1016/S0146-6380(99)00019-4.

Lovelock, C.E., Reef, R., 2020. Variable Impacts of Climate Change on Blue Carbon. One Earth 3, 195–211. https://doi.org/10.1016/j.oneear.2020.07.010.

Ma, Z., Zhao, S., Pan, Y., Li, Z., Liu, J., Zhang, M., Zhang, Z., 2024. Natural and regenerated saltmarshes exhibit different bulk soil and aggregate-associated organic and inorganic carbon contents but similar total carbon contents. J. Environ. Manage. 349, 119451 https://doi.org/10.1016/j.jenvman.2023.119451.

Macreadie, P.I., Costa, M.D.P., Atwood, T.B., Friess, D.A., Kelleway, J.J., Kennedy, H., Lovelock, C.E., Serrano, O., Duarte, C.M., 2021. Blue carbon as a natural climate solution. Nature Reviews Earth & Environment 2, 826–839. https://doi.org/10.1038/s43017-021-00224-1.

Matos, C.R.L., Berrêdo, J.F., Machado, W., Sanders, C.J., Metzger, E., Cohen, M.C.L., 2020. Carbon and nutrient accumulation in tropical mangrove creeks. Amazon Region. Marine Geology 429, 106317. https://doi.org/10.1016/j.margeo.2020.106317.

McKee, K.L., 1996. Growth and physiological responses of neotropical mangrove seedlings to root zone hypoxia. Tree Physiol. 16, 883–889. https://doi.org/10.1093/treephys/16.11-12.883.

McKee, K.L., Rooth, J.E., 2008. Where temperate meets tropical: multi-factorial effects of elevated CO 2, nitrogen enrichment, and competition on a mangrove-salt marsh community. Glob. Chang. Biol. 14, 971–984. https://doi.org/10.1111/j.1365-2486.2008.01547.x.

Mcleod, E., Chmura, G.L., Bouillon, S., Salm, R., Björk, M., Duarte, C.M., Lovelock, C.E., Schlesinger, W.H., Silliman, B.R., 2011. A blueprint for blue carbon: toward an improved understanding of the role of vegetated coastal habitats in sequestering CO_2. Front. Ecol. Environ. 9, 552–560. https://doi.org/10.1890/110004.

Midwood, A.J., Hannam, K.D., Gebretsadikan, T., Emde, D., Jones, M.D., 2021. Storage of soil carbon as particulate and mineral associated organic matter in irrigated woody perennial crops. Geoderma 403, 115185. https://doi.org/10.1016/j.geoderma.2021.115185.

Mirabito, A.J., Chambers, L.G., 2023. Quantifying mineral-associated organic matter in wetlands as an indicator of the degree of soil carbon protection. Geoderma 430, 116327. https://doi.org/10.1016/j.geoderma.2023.116327.

Nyman, J.A., Walters, R.J., Delaune, R.D., Patrick, W.H., 2006. Marsh vertical accretion via vegetative growth. Estuar. Coast. Shelf Sci. 69, 370–380. https://doi.org/10.1016/j.ecss.2006.05.041.

Osland, M.J., Day, R.H., Hall, C.T., Brumfield, M.D., Dugas, J.L., Jones, W.R., 2017a. Mangrove expansion and contraction at a poleward range limit: Climate extremes and land-ocean temperature gradients. Ecology 98, 125–137. https://doi.org/10.1002/ecy.1625.

Osland, M.J., Feher, L.C., Griffith, K.T., Cavanaugh, K.C., Enwright, N.M., Day, R.H., Stagg, C.L., Krauss, K.W., Howard, R.J., Grace, J.B., 2017b. Climatic controls on the global distribution, abundance, and species richness of mangrove forests. Ecol. Monogr. 87, 341–359. https://doi.org/10.1002/ecm.1248.

Osland, M.J., Feher, L.C., López-Portillo, J., Day, R.H., Suman, D.O., Guzmán Menéndez, J.M., Rivera-Monroy, V.H., 2018. Mangrove forests in a rapidly changing world: Global change impacts and conservation opportunities along the Gulf of Mexico coast. Estuar. Coast. Shelf Sci. 214, 120–140. https://doi.org/10.1016/j.ecss.2018.09.006.

Osland, M.J., Hartmann, A.M., Day, R.H., Ross, M.S., Hall, C.T., Feher, L.C., Vervaeke, W. C., 2019. Microclimate Influences Mangrove Freeze Damage: Implications for Range Expansion in Response to Changing Macroclimate. Estuar. Coasts 42, 1084–1096. https://doi.org/10.1007/s12237-019-00533-1.

Osland, M.J., Day, R.H., Michot, T.C., 2020. Frequency of extreme freeze events controls the distribution and structure of black mangroves (Avicennia germinans) near their northern range limit in coastal Louisiana. Divers. Distrib. 26, 1366–1382. https://doi.org/10.1111/ddi.13119.

Osland, M.J., Stevens, P.W., Lamont, M.M., Brusca, R.C., Hart, K.M., Waddle, J.H., Langtimm, C.A., Williams, C.M., Keim, B.D., Terando, A.J., Reyier, E.A., Marshall, K. E., Loik, M.E., Boucek, R.E., Lewis, A.B., Seminoff, J.A., 2021. Tropicalization of temperate ecosystems in North America: The northward range expansion of tropical organisms in response to warming winter temperatures. Glob. Chang. Biol. 27, 3009–3034. https://doi.org/10.1111/gcb.15563.

Ouyang, X., Lee, S.Y., Connolly, R.M., 2017. The role of root decomposition in global mangrove and saltmarsh carbon budgets. Earth Sci. Rev. 166, 53–63. https://doi.org/10.1016/j.earscirev.2017.01.004.

Patra, R., Saha, D., Jagadamma, S., 2022. Winter wheat cover crop increased subsoil organic carbon in a long-term cotton cropping system in Tennessee. Soil Tillage Res. 224, 105521 https://doi.org/10.1016/j.still.2022.105521.

Perry, C.L., Mendelssohn, I.A., 2009. Ecosystem effects of expanding populations of Avicennia germinans in a Louisiana salt marsh. Wetlands 29, 396–406. https://doi.org/10.1672/08-100.1.

Peterson, R.N., Burnett, W.C., Opsahl, S.P., Santos, I.R., Misra, S., Froelich, P.N., 2013. Tracking suspended particle transport via radium isotopes (226Ra and 228Ra) through the Apalachicola–Chattahoochee–Flint River system. J. Environ. Radioact. 116, 65–75. https://doi.org/10.1016/j.jenvrad.2012.09.001.

Picard, A., Gartman, A., Cosmidis, J., Obst, M., Vidoudez, C., Clarke, D.R., Girguis, P.R., 2019. Authigenic metastable iron sulfide minerals preserve microbial organic carbon in anoxic environments. Chem. Geol. 530, 119343 https://doi.org/10.1016/j.chemgeo.2019.119343.

Poeplau, C., Don, A., Six, J., Kaiser, M., Benbi, D., Chenu, C., Cotrufo, M.F., Derrien, D., Gioacchini, P., Grand, S., Gregorich, E., Griepentrog, M., Gunina, A., Haddix, M., Kuzyakov, Y., Kühnel, A., Macdonald, L.M., Soong, J., Trigalet, S., Vermeire, M.-L.,

Rovira, P., Van Wesemael, B., Wiesmeier, M., Yeasmin, S., Yevdokimov, I., Nieder, R., 2018. Isolating organic carbon fractions with varying turnover rates in temperate agricultural soils – A comprehensive method comparison. Soil Biol. Biochem. 125, 10–26. https://doi.org/10.1016/j.soilbio.2018.06.025.

Quisthoudt, K., Schmitz, N., Randin, C.F., Dahdouh-Guebas, F., Robert, E.M.R., Koedam, N., 2012. Temperature variation among mangrove latitudinal range limits worldwide. Trees 26, 1919–1931. https://doi.org/10.1007/s00468-012-0760-1.

R Development Core Team, 2023. R: a language and environment for statistical computing. R Foundation for Statistical Computing, Vienna, Austria.

Radabaugh, K.R., Moyer, R.P., Chappel, A.R., Powell, C.E., Bociu, I., Clark, B.C., Smoak, J.M., 2018. Coastal Blue Carbon Assessment of Mangroves, Salt Marshes, and Salt Barrens in Tampa Bay, Florida, USA. Estuar. Coasts 41, 1496–1510. https://doi.org/10.1007/s12237-017-0362-7.

Radabaugh, K.R., Moyer, R.P., Chappel, A.R., Breithaupt, J.L., Lagomasino, D., Dontis, E. E., Russo, C.E., Rosenheim, B.E., Chambers, L.G., Peneva-Reed, E.I., Smoak, J.M., 2023. A Spatial Model Comparing Above- and Belowground Blue Carbon Stocks in Southwest Florida Mangroves and Salt Marshes. Estuar. Coasts. https://doi.org/10.1007/s12237-023-01217-7.

Ransom, B., Kim, D., Kastner, M., Wainwright, S., 1998. Organic matter preservation on continental slopes: importance of mineralogy and surface area. Geochim. Cosmochim. Acta 62, 1329–1345. https://doi.org/10.1016/S0016-7037(98)00050-7.

Raven, M.R., Fike, D.A., Gomes, M.L., Webb, S.M., 2019. Chemical and Isotopic Evidence for Organic Matter Sulfurization in Redox Gradients Around Mangrove Roots. Front. Earth Sci. 7, 98. https://doi.org/10.3389/feart.2019.00098.

Riedel, T., Zak, D., Biester, H., Dittmar, T., 2013. Iron traps terrestrially derived dissolved organic matter at redox interfaces. PNAS 110, 10101–10105. https://doi.org/10.1073/pnas.1221487110.

Rietl, A.J., Overlander, M.E., Nyman, A.J., Jackson, C.R., 2016. Microbial Community Composition and Extracellular Enzyme Activities Associated with Juncus roemerianus and Spartina alterniflora Vegetated Sediments in Louisiana Saltmarshes. Microb. Ecol. 71, 290–303. https://doi.org/10.1007/s00248-015-0651-2.

Rocci, K.S., Barker, K.S., Seabloom, E.W., Borer, E.T., Hobbie, S.E., Bakker, J.D., MacDougall, A.S., McCulley, R.L., Moore, J.L., Raynaud, X., Stevens, C.J., Cotrufo, M.F., 2022. Impacts of nutrient addition on soil carbon and nitrogen stoichiometry and stability in globally-distributed grasslands. Biogeochemistry 159, 353–370. https://doi.org/10.1007/s10533-022-00932-w.

Rosentreter, J.A., Laruelle, G.G., Bange, H.W., Bianchi, T.S., Busecke, J.J.M., Cai, W.-J., Eyre, B.D., Forbrich, I., Kwon, E.Y., Maavara, T., Moosdorf, N., Najjar, R.G., Sarma, V.V.S.S., Van Dam, B., Regnier, P., 2023. Coastal vegetation and estuaries are collectively a greenhouse gas sink. Nat. Clim. Chang. 13, 579–587. https://doi.org/10.1038/s41558-023-01682-9.

Sánchez, J.M., 2010. Factors conditioning the vegetation in the salt marshes of the Atlantic coast of the Iberian Peninsula. Biogeochemistry and Pedogenetic Processes in Saltmarsh and Mangrove Systems 147.

Santos, I.R., Burdige, D.J., Jennerjahn, T.C., Bouillon, S., Cabral, A., Serrano, O., Wernberg, T., Filbee-Dexter, K., Guimond, J.A., Tamborski, J.J., 2021. The renaissance of Odum's outwelling hypothesis in "Blue Carbon" science. Estuar. Coast. Shelf Sci. 255, 107361 https://doi.org/10.1016/j.ecss.2021.107361.

Saraswati, S., Dunn, C., Mitsch, W.J., Freeman, C., 2016. Is peat accumulation in mangrove swamps influenced by the "enzymic latch" mechanism? Wetl. Ecol. Manag. 24, 641–650. https://doi.org/10.1007/s11273-016-9493-z.

Shields, M.R., Bianchi, T.S., Gélinas, Y., Allison, M.A., Twilley, R.R., 2016. Enhanced terrestrial carbon preservation promoted by reactive iron in deltaic sediments. Geophys. Res. Lett. 43, 1149–1157. https://doi.org/10.1002/2015GL067388.

Simpson, L.T., Lovelock, C.E., Cherry, J.A., Feller, I.C., 2020. Short-lived effects of nutrient enrichment on Avicennia germinans decomposition in a saltmarsh-mangrove ecotone. Estuar. Coast. Shelf Sci. 235, 106598 https://doi.org/10.1016/j.ecss.2020.106598.

Simpson, L.T., Cherry, J.A., Smith, R.S., Feller, I.C., 2021. Mangrove Encroachment Alters Decomposition Rate in Saltmarsh Through Changes in Litter Quality. Ecosystems 24, 840–854. https://doi.org/10.1007/s10021-020-00554-z.

Smoak, J.M., Breithaupt, J.L., Smith, T.J., Sanders, C.J., 2013. Sediment accretion and organic carbon burial relative to sea-level rise and storm events in two mangrove forests in Everglades National Park. Catena 104, 58–66. https://doi.org/10.1016/j.catena.2012.10.009.

Snyder, C.M., Feher, L.C., Osland, M.J., Miller, C.J., Hughes, A.R., Cummins, K.L., 2021. The Distribution and Structure of Mangroves (Avicennia germinans and Rhizophora mangle) Near a Rapidly Changing Range Limit in the Northeastern Gulf of Mexico. Estuar. Coasts 45, 181–195. https://doi.org/10.1007/s12237-021-00951-0.

Sokol, N.W., Sanderman, J., Bradford, M.A., 2019. Pathways of mineral-associated soil organic matter formation: Integrating the role of plant carbon source, chemistry, and point of entry. Glob Change Biol 25, 12–24. https://doi.org/10.1111/gcb.14482.

Sokol, N.W., Whalen, E.D., Jilling, A., Kallenbach, C., Pett-Ridge, J., Georgiou, K., 2022. Global distribution, formation and fate of mineral-associated soil organic matter under a changing climate: A trait-based perspective. Glob. Chang. Biol. 36, 1411–1429. https://doi.org/10.1111/1365-2435.14040.

Sollins, P., Swanston, C., Kleber, M., Filley, T., Kramer, M., Crow, S., Caldwell, B.A., Lajtha, K., Bowden, R., 2006. Organic C and N stabilization in a forest soil: Evidence from sequential density fractionation. Soil Biol. Biochem. 38, 3313–3324. https://doi.org/10.1016/j.soilbio.2006.04.014.

Spivak, A.C., Sanderman, J., Bowen, J.L., Canuel, E.A., Hopkinson, C.S., 2019. Global-change controls on soil-carbon accumulation and loss in coastal vegetated ecosystems. Nat. Geosci. 12, 685–692. https://doi.org/10.1038/s41561-019-0435-2.

H.E. Steinmuller E. Bourque S.B. Lucas K.M. Engelbert J. Garwood J.L. Breithaupt Comparing Vertical Change in Riverine, Bayside, and Barrier Island Wetland Soils in Response to Acute and Chronic Disturbance in Apalachicola Bay 2022 Estuaries and Coasts FL 10.1007/s12237-022-01131-4.

Steinmuller, H.E., Foster, T.E., Boudreau, P., Ross Hinkle, C., Chambers, L.G., 2020. Tipping Points in the Mangrove March: Characterization of Biogeochemical Cycling Along the Mangrove-Salt Marsh Ecotone. Ecosystems 23, 417–434. https://doi.org/10.1007/s10021-019-00411-8.

Steinmuller, H.E., Breithaupt, J.L., Engelbert, K.M., Assavapanuvat, P., Bianchi, T.S., 2022b. Coastal Wetland Soil Carbon Storage at Mangrove Range Limits in Apalachicola Bay, FL: Observations and Expectations. Frontiers in Forests and Global Change 5, 852910. https://doi.org/10.3389/ffgc.2022.852910.

Sun, H., Jiang, J., Cui, L., Feng, W., Wang, Y., Zhang, J., 2019. Soil organic carbon stabilization mechanisms in a subtropical mangrove and salt marsh ecosystems. Sci. Total Environ. 673, 502–510. https://doi.org/10.1016/j.scitotenv.2019.04.122.

Sun, R., Sun, B., Li, X., Wei, S., Zhao, M., Chu, X., Song, W., Yuan, J., Han, G., 2023. Seven-year experimental warming decreases labile but not recalcitrant soil organic carbon fractions in a coastal wetland. J. Soil. Sediment. 23, 3071–3081. https://doi.org/10.1007/s11368-023-03536-5.

Thibodeau, F.R., Nickerson, N.H., 1986. Differential oxidation of mangrove substrate by Avicennia germinans and Rhizophora mangle. Am. J. Bot. 73, 512–516. https://doi.org/10.1002/j.1537-2197.1986.tb12069.x.

Touchette, B.W., Smith, G.A., Rhodes, K.L., Poole, M., 2009. Tolerance and avoidance: Two contrasting physiological responses to salt stress in mature marsh halophytes Juncus roemerianus Scheele and Spartina alterniflora Loisel. J. Exp. Mar. Biol. Ecol. 380, 106–112. https://doi.org/10.1016/j.jembe.2009.08.015.

United States Department of Agriculture, 2023. Web Soil Survey. accessed 12.6.23. https://www.nrcs.usda.gov/resources/data-and-reports/web-soil-survey.

Vandenberghe, R.E., De Grave, E., 2012. Application of Mössbauer spectroscopy in earth sciences. Mössbauer Spectroscopy: Tutorial Book. Springer 91–185.

Vaughn, D.R., Bianchi, T.S., Shields, M.R., Kenney, W.F., Osborne, T.Z., 2020. Increased Organic Carbon Burial in Northern Florida Mangrove-Salt Marsh Transition Zones. Global Biogeochem. Cycles 34. https://doi.org/10.1029/2019GB006334.

Villarino, S.H., Pinto, P., Jackson, R.B., Piñeiro, G., 2021. Plant rhizodeposition: A key factor for soil organic matter formation in stable fractions. Sci. Adv. 7 https://doi.org/10.1126/sciadv.abd3176.

Wang, S., Jia, Y., Liu, T., Wang, Y., Liu, Z., Feng, X., 2021. Delineating the Role of Calcium in the Large-Scale Distribution of Metal-Bound Organic Carbon in Soils. Geophys. Res. Lett. 48 https://doi.org/10.1029/2021GL092391.

Wardinski, K.M., Hotchkiss, E.R., Jones, C.N., McLaughlin, D.L., Strahm, B.D., Scott, D. T., 2022. Water-soluble organic matter from soils at the terrestrial-aquatic interface in wetland-dominated landscapes. JGR Biogeosciences 127, e2022JG006994. https://doi.org/10.1029/2022JG006994.

Willemsen, P.W.J.M., Horstman, E.M., Borsje, B.W., Friess, D.A., Dohmen-Janssen, C.M., 2016. Sensitivity of the sediment trapping capacity of an estuarine mangrove forest. Geomorphology 273, 189–201. https://doi.org/10.1016/j.geomorph.2016.07.038.

Yang, W., An, S., Zhao, H., Xu, L., Qiao, Y., Cheng, X., 2016. Impacts of Spartina alterniflora invasion on soil organic carbon and nitrogen pools sizes, stability, and turnover in a coastal salt marsh of eastern China. Ecol. Eng. 86, 174–182. https://doi.org/10.1016/j.ecoleng.2015.11.010.

Yang, W., Zhao, H., Leng, X., Cheng, X., An, S., 2017. Soil organic carbon and nitrogen dynamics following Spartina alterniflora invasion in a coastal wetland of eastern China. Catena 156, 281–289. https://doi.org/10.1016/j.catena.2017.03.021.

Ye, C., Huang, W., Hall, S.J., Hu, S., 2022. Association of Organic Carbon With Reactive Iron Oxides Driven by Soil pH at the Global Scale. Global Biogeochem. Cycles 36. https://doi.org/10.1029/2021GB007128.

Yeasmin, S., Singh, B., Johnston, C.T., Sparks, D.L., 2017. Organic carbon characteristics in density fractions of soils with contrasting mineralogies. Geochim. Cosmochim. Acta 218, 215–236. https://doi.org/10.1016/j.gca.2017.09.007.

Yuan, Y., Zhang, Z., Chen, L., Yang, Z., Liu, J., 2022. Facilitated destabilization of physicochemically protected soil organic matter by root-derived low-molecular-weight organic acids. J. Soil. Sediment. 22, 1677–1686. https://doi.org/10.1007/s11368-022-03188-x.

Zhang, Y., Xiao, L., Guan, D., Chen, Y., Motelica-Heino, M., Peng, Y., Lee, S.Y., 2021. The role of mangrove fine root production and decomposition on soil organic carbon component ratios. Ecol. Ind. 125, 107525 https://doi.org/10.1016/j.ecolind.2021.107525.

Zhang, Y., Li, M., Zhang, J., Cui, J., Wang, X., Song, M., Qiao, Q., Long, X.-E., 2024. Spatial soil heterogeneity rather than the invasion of Spartina alterniflora drives soil bacterial community assembly in an Eastern Chinese intertidal zone along an estuary coastline. Catena 237, 107784. https://doi.org/10.1016/j.catena.2023.107784.

Zhao, Q., Poulson, S.R., Obrist, D., Sumaila, S., Dynes, J.J., McBeth, J.M., Yang, Y., 2016. Iron-bound organic carbon in forest soils: quantification andcharacterization. Biogeosciences 13, 4777–4788. https://doi.org/10.5194/bg-13-4777-2016.

Zhu, E., Liu, Z., Wang, S., Wang, Y., Liu, T., Feng, X., 2023. Organic Carbon and lignin protection by metal oxides versus silicate clay: comparative study based on wetland and upland soils. JGR Biogeosciences 128, e2023JG007474. https://doi.org/10.1029/2023JG007474.